Lavinia Gambelli[1,2], Benjamin Meyer[3], Mathew McLaren[1,2], Kelly Sanders[1,4], Tessa E.F. Quax[5], Vicki Gold[1,4], Sonja-Verena Albers[5] and Bertram Daum[1,4]*

[1] Living Systems Institute, University of Exeter, Exeter, United Kingdom
[2] College of Engineering, Mathematics and Physical Sciences, University of Exeter, Exeter, United Kingdom
[3] Molecular Enzymology, Faculty for Chemistry, University of Duisburg-Essen, Germany
[4] College of Life and Environmental Sciences, University of Exeter, Exeter, United Kingdom
[5] Institute of Biology II, Molecular Biology of Archaea, University of Freiburg, Freiburg, Germany

*Corresponding author

Architecture and modular assembly of the *Sulfolobus* S-layers revealed by electron cryo-tomography

Abstract

Surface protein layers (S-layers) often form the only structural component of the archaeal cell wall and are therefore important for cell survival. S-layers have a plethora of cellular functions including maintenance of cell shape, osmotic and mechanical stability, the formation of a semi-permeable protective barrier around the cell, cell-cell interaction, as well as surface adhesion. Despite the central importance of the S-layer for archaeal life, their three-dimensional architecture is still poorly understood. Here we present the first detailed 3D electron cryo-microscopy maps of archaeal S-layers from three different *Sulfolobus* strains. We were able to pinpoint the positions and determine the structure of the two subunits SlaA and SlaB. We also present a model describing the assembly of the mature S-layer.

Introduction

Many bacteria and archaea are surrounded by an outermost layer – the S-layer – which is composed of glycosylated surface proteins. These proteins arrange into flexible, porous, yet highly stable lattices that form cage-like coats around the plasma membrane. In bacteria, S-layers are anchored to the peptidoglycan or the outer membrane. In archaea, S-layers can be either incorporated into the periplasmatic polysaccharide layers such as pseudomurein and methanochondroitin, or simply integrated into the cytoplasmic membrane. In most cases, S-layers form ordered 2-dimensional arrays and serve a variety of functions, which are thought to be

specific to genera or groups of organisms sharing the same environment (Albers & Meyer, 2011; Engelhardt, 2007; Rodrigues-Oliveira, Belmok, Vasconcellos, Schuster, & Kyaw, 2017).

For archaea, S-layers are of particular importance as they often comprise the only cell wall component. They therefore define cellular shape and provide osmotic, thermal and mechanical stability (Engelhardt, 2007). In addition, *in vitro* experiments have shown that S-layers change the physical and biochemical properties of lipid layers, rendering them less flexible, less fluid, more stable and heat-resistant, and possibly more resistant to hydrostatic pressure. Furthermore, it has been suggested that S-layers provide protection against immunological defence systems and viruses, act as pathogenic virulence factors, serve as phage receptors, promote surface adhesion, establish a quasi-periplasmic space, provide anchoring scaffolds for membrane proteins, sequester ions and facilitate biomineralization (Engelhardt, 2007). S-layers are intrinsically capable of self-assembly *in vitro*, resulting in tube-like, spherical two-dimensional crystals (Dietmar Pum & Sleytr, 2014). S-layers are therefore highly interesting for various applications in nanotechnology (Sleytr et al., 2014).

Sulfolobus is a genus of hyperthermophilic acidophilic archaea, which grow in low-pH terrestrial hot springs at 75–80°C all around the globe. They are well-established model organisms, as they can be relatively easily cultured in the laboratory and the genomes of a number of strains have been sequenced (Chen et al., 2005; Kawarabayasi et al., 2001; She et al., 2009). The S-layer of all *Sulfolobus* species consists of two proteins, SlaA and SlaB. Biochemical analysis of SlaA and SlaB from different *Sulfolobus* species revealed molecular masses ranging from 120kDa - 180kDa or 40kDa - 45kDa, respectively (Grogan, 2010; Veith et al., 2009). Comparative sequence analysis and molecular modelling of SlaB revealed that it exists in two species-dependent variants. In *S. ambivalens*, *S. acidocaldarius*, *S. tokodaii* and *S. sedula,* SlaB is comprised of an N-terminal Sec-dependent signal sequence, followed by three consecutive beta-sandwich domains, an alpha-helical coiled coil domain and one C-terminal transmembrane helix. In contrast, the sequences of *S. solfataricus* and *S. islandicus* are shorter by one beta-sandwich domain (Veith et al., 2009). Interestingly, it was recently shown by negative stain electron microscopy (EM) that SlaB knockout strains of *S. islandicus* still assemble partial S-layers (Zhang et al., 2018).

In contrast, SlaA was predicted to be a soluble protein rich in beta-strands and to form the outer region of the *Sulfolobus* S-layer (Veith et al., 2009). Deletion mutants of SlaA led to deformed cells without a distinctive cell envelope (Zhang et al, 2018).

So far, the structure of the *Sulfolobus* S-layer has only been inferred by early 2D crystallography of negatively stained and isolated S-layers. These data suggested that Sulfolobus *S-layers* adopt a structurally conserved lattice with P3 symmetry, which encompasses 4,5 nm triangular and 8 nm hexagonal pores at a 21 nm distance (Baumeister & Lembcke, 1992; Taylor, Deatherage, & Amos, 1982). However, as detailed 3D maps were so-far unavailable, it has been unclear how SlaA und SlaB assemble into the final S-layer structure.

Using electron cryo-tomography (cryoET) and sub-tomogram averaging (STA), we obtained the first 3D cryoET maps of S-layers from three *Sulfolobus* species at unprecedented resolution. Through difference maps of fully-assembled and SlaB-depleted S-layers, we were able to unambiguously pinpoint the positions of the component subunits SlaA and SlaB. Based on these experiments, we present a 3D model describing their assembly. In addition, our data reveal that strain-specific variants of SlaB lead to marked differences in the outward-facing S-layer surface. We also find that SlaB is not required for SlaA S-layer assembly *in vitro*, which has important implications about the function of both S-layer components.

Results

In situ structure of the *Sulfolobus* S-layer

To obtain a first detailed understanding of the molecular architecture of the archaeal S-layer, we chose the *Sulfolobus* species *S. islandicus (Sisl)*, *S. solfataricus (Ssol)* and *S. acidocaldarius (Saci)*. In *Sisl* and *Ssol* the S-layer subunit proteins SlaA and SlaB show share 87.4% and 87.7% sequence identity (Fig. 1S1) and are thus virtually identical. In contrast, SlaA and SlaB from *Saci* show only ~24% or ~25 % identity with *Sisl / Ssol* (Fig. 1S2) and are thus far less conserved between those species. Moreover, SlaB from *Saci and Sisl/Ssol* have previously been proposed to represent two different structural “families” with respect to SlaB, which exists as a long form in *Saci* and a short form in *Ssol* and *Sisl* (Veith et al., 2009). We hypothesised that the two different variants of SlaA and SlaB may cause distinct S-layer geometries in *Saci* when compared to *Sisl* or *Ssol*.

To prepare cells for cryoET, cellular suspensions were plunge-frozen on holy carbon grids and investigated in the electron microscope. The majority of cells were surrounded by intact S-layers

100 and membranes and showed various degrees of cytoplasmic density, which may either be a result
101 of different metabolic states of slight cytosolic leakage during the sample preparation procedure.
102 Tomographic tilt series were collected of cells with low cytosolic density, which were more
103 transparent to the electron beam and thus resulted in tomograms with better signal-to-noise ratio
104 (Fig. 1A).
105
106 In tomographic reconstructions, cells appeared disk-shaped with a diameter of up to 2 µm and a
107 thickness of 250-300 nm (Fig. 1A). Since *Sulfolobus* cells are usually roughly spherical, this
108 suggests that the cells had been compressed due to surface tension of the buffer during the
109 plunge freezing procedure. In tomographic cross-sections, two layers confining the cells were
110 distinguished (Fig. 1A). Whereas the inner layer, the membrane, was smooth, the outer S-layer
111 had a corrugated appearance (Fig. 1B).
112 Tomographic sections parallel to the plane of the S-layers clearly showed that they indeed form
113 regular two-dimensional arrays, as confirmed by power spectra of the respective tomographic
114 slices. These power spectra showed clear spots up to the third order and indicated a lattice with
115 P3 symmetry (Fig. 1S3). The fuzzy spots indicated that the S-layers were not perfectly crystalline.
116 This was expected, as roughly round shapes cannot be contained in a hexagonal lattice unless
117 defects are included (D Pum, Messner, & Sleytr, 1991). Moreover, gaps in the lattice are needed
118 to accommodate surface filaments such as archaella (Daum et al., 2017) or to allow the cells to
119 grow and divide. In tomographic slices perpendicular to the membrane plane, S-layers formed
120 regular, corrugated canopy-like arrays at a centre-to-centre distance of ~30 nm from the
121 membrane (Fig. 1 B).
122
123 To obtain structural information of these S-layers in situ, 1809 subvolumes (*Sisl*) and 2068
124 subvolumes (*Saci)* were cut from tomograms, in which the cell surface was clearly resolved.
125 Subsequently, subvolumes were aligned and averaged in PEET. This resulted in 3D maps at ~30
126 Å and 28 Å resolution for *Sisl* and *Saci*, respectively (Fig. 1S5). Both S-layer maps revealed a
127 perforated two-dimensional protein lattice with P3 symmetry (Fig. 1; 1S4; 1S5). For *Sisl*, unit cell
128 dimensions were ~21.9 x 20.9 nm including an angle of 120° and for *Saci* the unit cell measured
129 ~23.9 x 23.6 nm with an angle of 120°. The unit cell of the *Saci* S-layer is therefore roughly 10 %
130 larger than that of *Sisl.* The total height of the maps was ~25 nm for *Sisl* and ~28 nm for *Saci*,
131 respectively (Fig. 1 D-G).
132

133 Our 3D maps revealed structurally conserved and unique features for both S-layers (Fig. 1 D-G).
134 In particular, the organisation of the inward-facing domains of the S-layer of both species are
135 generally the same. In either case, they consist of trimeric stalks (Fig. 1 blue and yellow). These
136 stalks support an outer canopy-like assembly (Fig. 1 D-G, green and red). At their membrane-
137 proximal parts, each of the trimeric stalks merge into a single protrusion, giving them a tulip-like
138 shape (Fig. 1 E, G blue and yellow). This protrusion most likely forms the membrane anchor of
139 the S-layer. Distal to the membrane, the stalks are connected to the S-layer canopy via their
140 trimeric domains.
141
142 The outer canopy forms the outward-facing side of the S-layer and resides on top of the array of
143 the trimeric stalks (Fig. 1 D-G). In *Sisl* and *Saci* the base of the canopy appears to be cross-linked
144 by a protein network, which has roughly the same in-plane geometry in both species (Fig. 1 D-G,
145 green). In cross-section perpendicular to plane of the S-layers, this network forms a continuous
146 band throughout the entire structure and includes repeating triangular and hexagonal pores. Two
147 types of triangular pores can be distinguished, of which one is situated on top of a trimeric stalk
148 (Fig. 1, E, G blue) while the other is not. The triangular pores with and without stalk alternate
149 throughout the lattice (Fig. 1 D-G).
150
151 The outward-facing part of the canopy is distinct in both species. In *Sisl,* it is composed of an
152 array of hexameric cone-shaped protrusions (Fig. 1 G, red). Each of the cones encloses a
153 hexagonal pore within the membrane. At their base, each cone is surrounded by six neighbouring
154 cones. The spaces between three cones contain the triangular pores (Fig 1 G).
155
156 In *Saci*, the most distal part of the outer layer is composed of elongated, petal-like structures (Fig.
157 1 D, red). As in *Saci* these structures do not protrude as far from the general plane of the canopy,
158 the outer S-layer face appears rather smooth compared to that of *Sisl*. As seen in Fig. 1 D, each
159 of these structures show a 2-fold symmetry around their long axis, which suggests that they are
160 dimers.
161
162 **Structural dissection of *Sulfolobus* S-layers**
163 To obtain higher resolution maps for *Sulfolobus* S-layers and to investigate if the cell context is
164 important to maintain correct S-layer assembly, we isolated S-layers – this time from *Saci* and
165 *Ssol,* the latter of which was by sequence alignments predicted to have the same shortened
166 domain structure as *Sisl.* Tomograms were recorded at optimised imaging conditions and sub-

167 tomogram averaging resulted in more detailed maps (Fig. 2) at 21 Å (*Saci*) and 16 Å (*Ssol*)
168 resolution (Fig. 1S5). The lattice parameters of the *Saci* S-layer remained unchanged, showing
169 that their integrity does not crucially depend on the cellular context (Fig. 2 A). Moreover, the map
170 of the *Ssol* S-layer was virtually identical to the one of *Sisl* in terms of lattice dimensions and outer
171 canopy topology (Fig. 2 B), indicating that 87 % sequence identity conserves the general
172 structural features.
173
174 To further investigate the structural differences between *Saci* and *Ssol*, we segmented each map
175 into units composed of three stalks and the adjacent canopy (Fig 2 C, D). As with *Sisl*, the S-layer
176 of *Ssol* clearly showed a smaller unit size of 10 % when compared to the one of *Saci*. Furthermore,
177 structural differences surrounding the hexagonal pores were resolved more clearly. Whereas in
178 *Saci* each hexagonal pore is flanked by six inward-curled protein domains, it is surrounded by six
179 outward projecting densities in *Ssol,* giving rise to the cone-like assemblies.
180
181 **Pinpointing SlaA and SlaB**
182 In order to locate SlaA and SlaB within the *Sulfolobus* S-layer, we first removed the subunit SlaB
183 from isolated S-layers using the detergent N-laurylsarcosine (Fig. 3 A). After 3-4 repeated
184 washing steps, this subunit ceased to be detectable by SDS PAGE. CryoET and sub-tomogram
185 averaging of the SlaB-depleted S-layer resulted in a map that lacked the trimeric stalks (Fig 3 C),
186 leaving behind the porous canopy. This clearly indicates that SlaB constitutes the trimeric stalks
187 that anchor the S-layer in the membrane. Consequently, the canopy must be formed by SlaA,
188 which is in line with previous predictions (Veith et al., 2009).
189 To visualise the location and architecture of SlaB unambiguously, we calculated a difference map
190 by subtracting the SlaB-depleted from the fully assembled map (Fig. 3 D). This revealed that SlaB
191 adopts a tripod-like shape, which is consistent with earlier sequence-based predictions that
192 suggested that SlaB foms a trimer (Veith et al., 2009). In our structure, the three branches of each
193 SlaB trimer are buried inside the SlaA canopy, whilst the “monomeric” stalk projects away from it,
194 towards the membrane plane. In multitude, these pillars act to raise the SlaA canopy above the
195 membrane. Interestingly, individual SlaB units are not in contact, but are linked to each other via
196 the SlaA canopy network. Notably, the canopy structure of the SlaB-depleted S-layer was less
197 well resolved than in the fully-assembled control sample (Fig. 3 B). This suggests that SlaB may
198 act in reinforcing the stability of the SlaA network.
199
200

201 **Role of SlaB in S-layer assembly**

202 As the S-layer structure is maintained after removal of SlaB, we asked if SlaB proteins merely
203 function as pillars for the SlaA lattice or if they also aide correct assembly of the outer canopy. To
204 investigate this, we isolated S-layers from both *Saci* and *Ssol*, disassembled them by transfer into
205 pH 10 buffer and subsequently performed recrystallisation by dialysis against water at pH 7 and
206 incubation for 120 h. Inspection of the reaction containing both subunits in the electron
207 microscope revealed patches of reassembled S-layers (Fig. 4 A, D). Sub-tomogram averaging
208 showed that these S-layers had retained their original lattice dimensions (Fig. 4 B, E) and that the
209 SlaA canopy as well as SlaB stalks could be identified (Fig. 4 C, F).

210

211 Interestingly, electron microscopy of the SlaB-depleted samples also revealed newly-formed S-
212 layers (Fig. 4 G, H, J, K). Again, sub-tomogram averaging confirmed that the reassembled S-
213 layers had adopted their original lattice parameters, however this time without the SlaB stalks
214 (Fig. 4 I and L). These observations indicate that SlaB is not involved in assembly process of the
215 SlaA canopy and suggests that it mainly functions as a membrane anchor and distance ruler that
216 determines the width of the periplasmic space.

217

218 **Assembly model of the *Sulfolobus* S-layer**

219 It has previously been shown biochemically and confirmed by us that SlaA forms a stable ~250
220 kDa dimer in solution (Veith et al., 2009). In conjunction with early electron microscopy, it has also
221 been predicted that this dimer forms the primary *Sulfolobus* S-layer building block (Taylor et al.,
222 1982; Veith et al., 2009). This repeating dimer-array is apparent in our sub-tomogram averages
223 of negatively-stained SlaA-only S-layers (Fig. 4 I). To build a cryoEM model of the *Saci* and *Ssol*
224 S-layers, we first segmented the SlaB-depleted sub-tomogram averaging maps by the water-
225 shedding method in Chimera (Pettersen et al., 2004). For guidance, we used the constraints of
226 repeating dimeric SlaA densities that roughly fitted the molecular weight of 250 kDa, as well as
227 our negative stain map in which the individual dimers were clearly visible (Fig. 4 I). We then
228 superimposed this segmentation with the fully-assembled S-layer, which provided us with the
229 positions of SlaB trimers.

230

231 The resulting model shows the location of SlaA dimers and SlaB trimers within the assembled S-
232 layers of *Saci* (Fig. 5 A-C) and *Ssol* (Fig. 5 D-F). In both cases, individual SlaA dimers adopt the
233 shape of a boomerang. The elbow of each boomerang interacts with one of the three branches
234 of a SlaB trimer, whereas both SlaA arms project outward. Thus, each SlaB trimer is bound to

three SlaA dimers ($SlaB_3/3SlaA_2$), which intersect to form a triangular pore above each SlaB trimer. Three of these flower-shaped $SlaB_3/3SlaA_2$ surround one hexagonal pore, formed by six SlaA dimers. Herein, each of the three SlaB trimers contributes 2 SlaA dimers to the hexameric ring. At the same time, each SlaA dimer spans two neighbouring hexameric pores. The second triangular pore type that does not coincide with a SlaB trimer is formed by three intersecting SlaA dimers at the interface of three hexagonal pores. In total, each SlaA dimer interacts with four SlaA dimers and 3 SlaB trimers. Therefore, SlaA dimers interlink into a tightly woven S-layer canopy that is stabilised by multiple interactions.

SlaA determines S-layer geometry and topology

To understand how *Saci* and *Ssol* assemble S-layers with similar geometry but different topology and unit cell size, we compared the structures of the SlaA proteins from each species. To this end, we extracted individual dimer densities from our segmented maps shown in Fig. 5.

This comparison revealed that while the overall shape of the dimers is the same, there are marked differences with respect to their horizontal and vertical dimensions, as well as the angles between both arms of each boomerang (Fig 6). *Saci* SlaA measures 23 nm along its long axis, which corresponds with the size of the unit cell of the S-layer (Fig 6A). This is to be expected, as this molecule spans to neighbouring hexagonal S-layer pores (Fig. 6C). The corresponding portion of *Ssol* SlaA measures ~20 nm (Fig. 6B), which is again in accordance with the 10% smaller assembled array (Fig 6D). The length of the SlaA dimer therefore determines the size of the unit cell. The differences in length appear to be established by the angle between both arms of the molecule, which is 102° for the longer *Saci* SlaA and 96° for the shorter *Ssol* homolog. Interestingly, both SlaA variants also differ in an apical domain, which is curled inwards in *Saci* and projects upwards in *Ssol*. In assembly, these domains are responsible for the differences in the topology of both S-layers, as it is these domains that delineate the shallow hexagonal pores in S*aci* and the conical protrusions in *Ssol* (Fig. 6 C, D). Taken together, the strain-specific dimensions and surface morphology of *Sulfolobus* S-layers are determined by unique structural characteristics of SlaA, in particular its apical domains.

Discussion

Roles of SlaA and SlaB in S-layer assembly

In this study, we describe the first cryoET-based molecular maps of archaeal S-layers. These maps unambiguously show that the *Sulfolobus* S-layer consists of trimeric SlaB proteins that adopt tripod-like structures and act as pillars that anchor the outer S-layer canopy in the cell membrane. The building block of the S-layer canopy is a dimer of SlaA, which assembles into a porous array of P3 symmetry. These observations are consistent with earlier predictions based on sequence analysis, biochemistry and early negative-stain electron microscopy maps (Baumeister & Lembcke, 1992; Taylor et al., 1982; Veith et al., 2009).

While X-ray structures for neither of the component proteins are available, sequence predictions indicated that SlaA and SlaB contain Sec-dependent signal peptides and are thus translocated through the membrane by the general secretory pathway. In addition, glycoproteomic analysis showed that both proteins contain several sites for N- and O-linked glycosylation and are heavily glycosylated prior to assembly (Palmieri et al., 2013; Peyfoon et al., 2010) (Fig. 7). Moreover, SlaB has been predicted to consist of an N-terminal membrane-anchor, followed by coiled-coil domain including a serine and threonine-rich highly-glycosylated region (ST linker) and 2-3 C-terminal beta sandwich domains (Veith et al., 2009) (Fig. 7). Upon trimerisation of SlaB, three C-termini presumably form a trimeric coiled-coil, which most likely corresponds to the stalk-like base of each SlaB tripod (Fig. 7). The SlaB stalks in our maps appear shorter than expected for a coiled-coil of roughly 100 amino acids (Veith et al., 2009) in length. This is likely due to high flexibility in this region, which is thus mostly averaged out during our sub-tomogram averaging procedure. The three protrusions of each SlaB tripod are likely formed by the predicted C-terminal beta-sandwich domains (Veith et al., 2009) of the three SlaB proteins in the trimer, which therefore also form the interface with the overarching SlaA lattice (Fig. 7). However due to the limited resolution of our maps, we were unable to distinguish between the length differences in the *Saci* and *Ssol* SlaB beta-sandwich domains.

Our reassembly experiments reveal that SlaB is not required for SlaA self-assembly *in vitro*. This is consistent with recent whole-cell negative stain EM data, which showed that *Sisl* SlaB knockout strains still assemble partial S-layer like coats (Zhang et al., 2018). We therefore conclude that the SlaA protein is the driving factor of S-layer assembly. In addition, our data shows that strain-specific S-layer surface features including lattice dimensions and topology, are determined by the shape of SlaA.

303 In contrast, SlaB's main function is to serve as a membrane anchor, distance ruler and to create
304 the periplasmic space. This space has been proposed to have important roles in archaeal cell
305 biology, including the coordination of membrane-embedded molecular machines, such as the
306 archaellum (Banerjee et al., 2015; Daum et al., 2017) and various other archaeal surface
307 structures (Chaudhury, Quax, & Albers, 2018). Secondarily, we observe that SlaA-only S-layers
308 are slightly less ordered than their fully-assembled counterparts, indicating that SlaB also
309 increases the stability of the S-layer, presumably by crosslinking $3SlaA_2$ subcomplexes with each
310 other.
311
312 The functional significance of the different S-layer topologies is largely unknown and awaits
313 further exploration. It may be speculated that distinct S-layer surface structures have evolved to
314 modulate the cell-adhesive properties of different archaeal strains. In addition, S-layers may act
315 as receptors in cell-cell recognition or phage infection (Plaut et al., 2014) and we could show
316 previously that archaeal viruses evolved elaborate cell entry and egress strategies to overcome
317 the S-layer barrier (Daum et al, 2013; Quemin et al, 2014; Quax & Daum 2018). It is therefore
318 conceivable that distinct S-layer topologies provide unique recognition tags for strain-specific
319 interaction and communication and that the evolution of new structures is a manifestation of the
320 cell's strategy to avoid viral infection (Tschitschko et al, 2015). SlaB, in contrast, appears
321 structurally more conserved than SlaA. Indeed, it has been shown previously that SlaB proteins
322 have lower sequence variability than SlaA and their molecular masses differ less across different
323 *Sulfolobus* strains (Veith et al., 2009). This is likely due to the fact that SlaB interacts less with the
324 extracellular medium and is thus less prone to environmentally-related evolutionary pressures.
325
326 Recently, an additional paralogous SlaB gene product (M164_1049, SSO1175 or
327 WP_011278654.1 in *Sisl*, *Ssol,* or *Saci*, respectively) was suggested to form another membrane-
328 anchored protein component of the *Sulfolobus* S-layer (Zhang et al, 2018). Double M164_1049
329 and SlaB mutants showed that no S-layer is present in *Sisl*, as opposed to single SlaB mutants
330 where a partial coat of SlaA was observed. In addition, a single M164_1049 deletion mutant
331 showed virtually no difference compared to the wild type. It was concluded that M164_1049 may
332 aid in anchoring SlaA to the cytoplasmic membrane (Zhang et al., 2018). Based on our maps, we
333 cannot confirm the presence of this protein. As it is membrane-anchored, it likely resides near the
334 membrane plane, the region which is averaged out in our data due to the highly flexible nature of
335 the SlaB coiled-coil domain.

336 In contrast to *Sulfolobus,* many archaeal strains possess only one S-layer protein. For example,
337 in many haloarchaea, a single S-layer glycoprotein (gene product *csg1* / SLG protein in *Haloferax*
338 *volcanii*) combines membrane-anchoring and canopy-forming functions into one protein.
339 Moreover, this protein is not membrane-integral but instead inserted to the bilayer via a C-terminal
340 lipid anchor (Fig. 7) (Pohlschroder, Pfeiffer, Schulze, & Halim, 2018). While employing only one
341 S-layer protein might be energetically more favorable, it is likely that using two increases the
342 adaptability of the S-layer surface (SlaA) without compromising the membrane anchor (SlaB).

343

344 **Function of S-layer pores**

345 One of the most striking features of the *Saci* and *Ssol* S-layers are the circular apertures of ~4.5
346 or ~8 nm in diameter that repeat throughout the array. Similar porous, skeleton-like architectures
347 have been reported for other S-layers such as that of the bacterium *Caulobacter cresentus*
348 (Bharat et al., 2017), highlighting that S-layer porosity is a highly conserved trait throughout
349 bacterial and archaeal species and thus provides a significant evolutionary advantage. This poses
350 the question what function these openings may convey. It is likely that – similar to chainmail - this
351 skeleton-like structure enhances S-layer flexibility, enabling it to coat cell bodies of various shape
352 and allowing the cell to morph and divide. It is also tantalising to assume that the particular shape
353 and size of the pores has evolved to accommodate particular cellular filaments, such as adhesive
354 pili or archaella. In contrast to this notion, we find that most known archaeal surface filaments,
355 such as adhesive (AAP) pili (Braun et al., 2016; Henche et al., 2012) and archaella (Daum et al.,
356 2017; Poweleit et al., 2016) are over 10 nm in diameter and thus too wide to be accommodated
357 by S-layer pores. Thus, the S-layer will have to be partially disassembled or adopt a different local
358 geometry wherever these filaments emerge from the cell body (Daum et al., 2017). Finally, it is
359 safe to assume that due to their porosity, S-layers provide a semi-permeable barrier, similar to
360 the outer membrane of Gram-negative bacteria, albeit with a more liberal molecular weight cut-
361 off. At the first glance, this cut-off appears to be determined by the pore diameter (<8nm), which
362 would allow a large variety of solutes, macromolecules and even large proteins to pass. However,
363 this notion may be deceptive, as both SlaA and SlaB are highly glycosylated (Palmieri et al., 2013;
364 Peyfoon et al., 2010). While (likely due to their high flexibility) these posttranslational modifications
365 are averaged out in our cryoEM maps, they are thought to cover much of the S-layer surface and
366 thus possibly also project into the pores (Fig. 7). It is conceivable that these glycans would
367 significantly lower the permeability of the S-layer pores to macromolecules, similar to the hydrogel
368 found in nuclear pore complexes (D'Angelo & Hetzer, 2008).

369 ## Conclusions

370 We present the first detailed 3D models of S-layers of three different *Sulfolobus* strains and
371 pinpoint the location and organisation of their component subunits SlaA and SlaB. We find that
372 the structure of the SlaA dimer determines the unit cell size and topology of the S-layer, whilst
373 SlaB anchors the S-layer in the plasma membrane and defines a pseudo-periplasmic space.
374 Different S-layer topologies between species are likely the result of various evolutionary
375 adaptations, including cell-cell interactive specificity and adhesive properties. Despite being an
376 ubiquitous hallmark in archaea, many functional aspects of S-layers still need to be clarified
377 through further structural investigation.
378

379 ## Materials and Methods

380

381 **Strains and growth conditions**

382 The strains *Ssol* and *Saci* MW001 were grown in basal Brock medium* at pH 3 (Brock, 1972).
383 The medium was supplemented with 0.1 % (w/v) NZ-amine and 0.2 % (w/v) dextrin just before
384 inoculation. For growth of *Saci* MW001, 10 µg/ml uracil was added to the medium. *Sulfolobus*
385 cultures were grown at 75°C, 150 rpm, until an OD600 of > 0.6 was reached. Cells were harvested
386 by centrifugation at 5000 x g (Sorvall ST 8R) for 30 min and stored at -20°C for subsequent use.
387

388 * Brock media contains (amount per litre): 1.3 g $(NH_4)_2SO_4$, 0.28 g KH_2PO_4, 0.25 g $MgSO_4$ ×
389 $7H_2O$, 0.07 g $CaCl_2$ × $2H_2O$, 0.02 g $FeCl_2$ × $4H_2O$, 1.8 mg $MnCl_2$ × $4H_2O$, 4.5 mg $Na_2B_4O_7$ ×
390 $10H_2O$, 0.22 mg $ZnSO_4$ × $7H_2O$, 0.05 mg $CuCl_2$ × $2H_2O$, 0.03 mg $NaMoO_4$ × $2H_2O$, 0.03 mg
391 $VOSO_4$ × $2H_2O$ and 0.01 mg $CoSO_4$ × $7H_2O$.
392

393 **S-layer isolation**

394 Cell pellets of frozen cells from a 50 ml culture were incubated and inverted on a rotator at 40 rpm
395 (Stuart SB3) for 45 min at 37°C, in 40 ml of buffer A (10 mM NaCl, 1 mM phenylmethylsulfonyl
396 fluoride, 0.5 % sodium lauroylsarcosine), with the addition of 10 µg/ml DNAse I just prior to use.
397 The samples were pelleted by centrifugation at 18.000 x g (Sorvall Legend XTR) for 30 min, and
398 subsequently resuspended in 1.5 ml buffer A, before further incubation and inversion at 37°C, for
399 30 min. After centrifugation at 14.000 rpm for 30 min (Sorvall ST 8R), the pellet was purified by
400 resuspension and incubation in 1.5 ml buffer B (10 mM NaCl, 0.5 mM $MgSO_4$, 0.5% SDS) and
401 rotated for 20 min at 37°C, 40 rpm. To retain both SlaA and SlaB, only one wash was performed.

402 To remove SlaB, washing with buffer B was repeated a further three times. Purified S-layer
403 proteins were washed once with distilled water and stored at 4°C. The removal of SlaB was
404 confirmed by SDS-PAGE analysis.
405
406 **Disassembly and reassembly of S-layers**
407 S-layers were disassembled by increasing the pH with the addition of 20 mM $NaCO_3$, pH 10, 10
408 mM $CaCl_2$ and incubation at 60°C, 600 rpm (Thermomixer F1.5, Eppendorf) for 1h. Disassembly
409 was verified by SDS-PAGE analysis.
410
411 Reassembly was achieved by buffer exchange using 0.5 ml concentrators according to the
412 manufacturer's instructions (Pierce), with dH_2O to reduce the pH to 7, followed by the addition of
413 10mM $CaCl_2$ and incubation at 60°C for 120 hours.
414
415 **Negative stain tomography**
416 A 3 µl sample of S-layers with and without SlaB was placed on glow-discharged carbon-coated
417 copper grids (Agar Scientific) and incubated at room temperature for 1 min. The excess sample
418 was removed by blotting using filter paper (Whatman, GH healthcare). The specimens were
419 stained using ammonium molybdate for 1 min. Grids were blotted dry with filter paper and let air
420 dry completely. Single axis tilt series (-60 to +60) were recorded on a FEI T12 electron microscope
421 operated at 120 kV, using DigitalMicrograph (Gatan Inc.).
422 Tilt series were reconstructed using the IMOD package (Kremer et al, 1996) and tomograms were
423 generated using the weighted back-projection algorithm.
424
425 **Electron cryo-tomography**
426 3 µl of S-layer suspension were applied to glow-discharged 300 mesh copper Quantifoil grids
427 (R2/2, Quantifoil, Jena, Germany), blotted for 3 – 5 seconds and rapidly injected into liquid ethane
428 using a homemade plunge-freezer. Tomograms were recorded using a Polara G2 Tecnai
429 (Thermo-Fisher, Eindhoven, The Netherlands) or a Jeol 3200 FSC TEM (JEOL, Tokyo, Japan),
430 both based at the Max Planck Institute of Biophysics in Frankfurt, Germany. The microscopes
431 were operated at 300 kV. Data were collected using a 4 x 4 k CCD camera or a 4x4 k K2 Summit
432 direct electron detector (Gatan Inc., Pleasanton, USA) running in counting mode. Inelastically
433 scattered electrons were removed using a Gatan Tridiem energy filter (Gatan Inc., Pleasanton,
434 USA) for the Polara and an in-column energy filter for the JEOL microscope. Tilt series were
435 collected in zero-loss mode using Digital Micrograph (Gatan, Pleasonton, USA) from -62° to +62°

436 and in steps of 2°. For tomograms of whole cells, the Polara was used. The magnification was set
437 to 41.000 x (resulting in a final pixel size of 5.4 Å on the final image) and defocus values of 6-8
438 µm were applied. For isolated S-layers, the magnification used was 72.000 (final image pixel of
439 2.8 Å) on the Polara and 10.000 x (final pixel size 3.35) on the JEOL. Defocus values of 2-4 µm
440 were used. Whole-cell tomograms were recorded using a CCD camera with a total dose of 100
441 e^{-} $Å^{-2}$. Tomograms of isolated S-layers were recorded using the K2 and in dose-fractionation mode
442 at a dose rate of 8-10 e^{-} px^{-1} s^{-1} and a maximum total dose of 60 e^{-} $Å^{-2}$. Dose-fractionated tilt
443 images were aligned using an in-house script based on IMOD (Kremer et al, 1996) programmes,
444 CTF corrected and reconstructed into tomograms using the IMOD software package (Kremer et
445 al, 1996).
446
447 **Sub-tomogram averaging**
448 To average the S-layer, a random grid of points was applied over the S-layer within a tomograms
449 of *Sulfolobus* cells or isolated S-layers, which were previously binned twofold. Whole-cell
450 tomograms were filtered by NAD (Frangakis and Hegerl, 2001) to enhance the contrast. Using
451 PEET (Nicastro et al, 2006; Heumann et al, 2011), subvolumes were extracted, aligned and
452 averaged. For the *in situ* S-layer average, 1809 subvolumes (*Sisl*) and 2068 subvolumes (*Saci)*
453 of 60x60x60 pixels in dimension were used. For isolated S-layers, 325 subvolumes (*Saci)* and
454 5561 subvolumes (*Ssol)* of 100 x 100 x 80 were used. P3 symmety was applied to the final
455 averages. S-layers were visualised and segmented using UCSF Chimera (Pettersen et al, 2004).
456 The resolution of all averages was estimated based the reflections in their respective power
457 spectra calculated by IMOD (Kremer et al, 1996). For the *in situ* structures this suggested a
458 resolution of 28 Å for *Saci* and 30 Å for *Sisl*. For the maps of the isolated S-layers, 16 Å were
459 measured for *Ssol* and 21 Å for *Saci* (Fig. 1S5).
460
461 **Difference maps and assembly models**
462 The difference maps were calculated and assembly models built in UCSF Chimera (Pettersen et
463 al, 2004). To calculate the difference map between the fully assembled and SlaB-depleted S-
464 layers, the *vop subtract* command was used. This resulted in clear densities for SlaB trimers. To
465 build the assembly model of the SlaA canopy regions, semi-automated water-shedding
466 segmentation was initially used on the sub-tomogram average of the SlaB-depleted S-layers. This
467 approach segmented the map in equal-sized parts, which were then grouped to generate a P3
468 lattice of dimers. Individual SlaB and SlaA subunits were extracted as separate densities from the

map and fitted into the fully assembled *Ssol and Saci* S-layers to yield the complete SlaA/SlaB assembly model.

Sequence alignments

Protein sequences were sourced online using Uniprot (https://www.uniprot.org/) and multiple sequence alignments performed with the Praline Server (http://www.ibi.vu.nl/programs/pralinewww/)

Acknowledgements

We thank Werner Kühlbrandt and Deryck Mills (MPI of Biophysics in Germany) for allowing us to use the Polara electron microscope. This project was funded by the Max Planck Society (BD), the University of Exeter Research Fellow's Startup grant (BD) and the ERC starting grant "MICROROBOTS" (BD, LG, MM, KS).

References

Albers, S. V., & Meyer, B. H. (2011). The archaeal cell envelope. *Nature Reviews Microbiology*. https://doi.org/10.1038/nrmicro2576

Banerjee, A., Tsai, C. L., Chaudhury, P., Tripp, P., Arvai, A. S., Ishida, J. P., … Albers, S. V. (2015). FlaF is a beta-sandwich protein that anchors the archaellum in the archaeal cell envelope by binding the S-layer protein. *Structure*, *23*(5), 863–872. https://doi.org/10.1016/j.str.2015.03.001

Baumeister, W., & Lembcke, G. (1992). Structural features of archaebacterial cell envelopes. *Journal of Bioenergetics and Biomembranes*. https://doi.org/10.1007/BF00762349

Bharat, T. A. M., Kureisaite-Ciziene, D., Hardy, G. G., Yu, E. W., Devant, J. M., Hagen, W. J. H., … Löwe, J. (2017). Structure of the hexagonal surface layer on Caulobacter crescentus cells. *Nature Microbiology*. https://doi.org/10.1038/nmicrobiol.2017.59

Braun, T., Vos, M. R., Kalisman, N., Sherman, N. E., Rachel, R., Wirth, R., … Egelman, E. H. (2016). Archaeal flagellin combines a bacterial type IV pilin domain with an Ig-like domain. *Proceedings of the National Academy of Sciences*, *113*(37), 10352–10357. https://doi.org/10.1073/pnas.1607756113

501 Chaudhury, P., Quax, T. E. F., & Albers, S. V. (2018). Versatile cell surface structures of
502 archaea. *Molecular Microbiology*. https://doi.org/10.1111/mmi.13889
503 Chen, L., Brügger, K., Skovgaard, M., Redder, P., She, Q., Torarinsson, E., … Garrett, R.
504 A. (2005). The genome of Sulfolobus acidocaldarius, a model organism of the
505 Crenarchaeota. *Journal of Bacteriology*. https://doi.org/10.1128/JB.187.14.4992-
506 4999.2005
507 D'Angelo, M. A., & Hetzer, M. W. (2008). Structure, dynamics and function of nuclear pore
508 complexes. *Trends in Cell Biology*. https://doi.org/10.1016/j.tcb.2008.07.009
509 Daum, B., Vonck, J., Bellack, A., Chaudhury, P., Reichelt, R., Albers, S.-V., … Kühlbrandt,
510 W. (2017). Structure and *in situ* organisation of the *Pyrococcus furiosus* archaellum
511 machinery. *ELife*, *6*. https://doi.org/10.7554/eLife.27470
512 Daum, B., Quax, T.E.F., Sachse, M., Mills, D., Reimann, J., Yildiz, Ö., Häder, S., Saveanu,
513 C., Forterre, P., Albers, S.V., Kühlbrandt, W. and Prangishvili, D. (2014). Self-
514 assembly of the universal membrane-remodeling protein PVAP into 7-fold virus-
515 associated pyramids. Proceedings of the National Academy of Sciences of the United
516 States of America, 111(10):3829-34. https://doi.org/10.1073/pnas.1319245111
517 Engelhardt, H. (2007). Are S-layers exoskeletons? The basic function of protein surface
518 layers revisited. *Journal of Structural Biology*, *160*(2), 115–124.
519 https://doi.org/10.1016/j.jsb.2007.08.003
520 Grogan, D. W. (2010). Organization and interactions of cell envelope proteins of the
521 extreme thermoacidophile Sulfolobus acidocaldarius . *Canadian Journal of*
522 *Microbiology*. https://doi.org/10.1139/m96-148
523 Henche, A. L., Ghosh, A., Yu, X., Jeske, T., Egelman, E., & Albers, S. V. (2012). Structure
524 and function of the adhesive type IV pilus of Sulfolobus acidocaldarius. *Environmental*
525 *Microbiology*. https://doi.org/10.1111/j.1462-2920.2012.02898.x
526 Kawarabayasi, Y., Hino, Y., Horikawa, H., Jin-No, K., Takahashi, M., Sekine, M., …
527 Kikuchi, H. (2001). Complete genome sequence of an aerobic thermoacidophilic
528 crenarchaeon, Sulfolobus tokodaii strain. *DNA Research*.
529 https://doi.org/10.1093/dnares/8.4.123
530 Palmieri, G., Balestrieri, M., Peter-Katalinić, J., Pohlentz, G., Rossi, M., Fiume, I., &
531 Pocsfalvi, G. (2013). Surface-exposed glycoproteins of hyperthermophilic sulfolobus
532 solfataricus P2 show a common N- glycosylation profile. *Journal of Proteome*
533 *Research*. https://doi.org/10.1021/pr400123z

534 Pettersen, E. F., Goddard, T. D., Huang, C. C., Couch, G. S., Greenblatt, D. M., Meng, E.
535 C., & Ferrin, T. E. (2004). UCSF Chimera: A visualization system for exploratory
536 research and analysis. *Journal of Computational Chemistry*, *25*(13), 1605–1612.
537 https://doi.org/10.1002/jcc.20084
538 Peyfoon, E., Meyer, B., Hitchen, P. G., Panico, M., Morris, H. R., Haslam, S. M., … Dell, A.
539 (2010). The S-layer glycoprotein of the crenarchaeote Sulfolobus acidocaldarius is
540 glycosylated at multiple sites with chitobiose-linked N-glycans. *Archaea*.
541 https://doi.org/10.1155/2010/754101
542 Plaut, R. D., Beaber, J. W., Zemansky, J., Kaur, A. P., George, M., Biswas, B., …
543 Sozhamannan, S. (2014). Genetic evidence for the involvement of the S-Layer protein
544 gene Sap and the sporulation genes spo0A, spo0B, and spo0F in phage AP50c
545 infection of Bacillus anthracis. *Journal of Bacteriology*.
546 https://doi.org/10.1128/JB.00739-13
547 Pohlschroder, M., Pfeiffer, F., Schulze, S., & Halim, M. F. A. (2018). Archaeal cell surface
548 biogenesis. *FEMS Microbiology Reviews*. https://doi.org/10.1093/femsre/fuy027
549 Poweleit, N., Ge, P., Nguyen, H. H., Loo, R. R. O., Gunsalus, R. P., & Zhou, Z. H. (2016).
550 CryoEM structure of the Methanospirillum hungatei archaellum reveals structural
551 features distinct from the bacterial flagellum and type IV pili. *Nature Microbiology*, *2*,
552 16222. https://doi.org/10.1038/nmicrobiol.2016.222
553 Pum, D, Messner, P., & Sleytr, U. B. (1991). Role of the S layer in morphogenesis and cell
554 division of the archaebacterium Methanocorpusculum sinense. *Journal of*
555 *Bacteriology*, *173*(21), 6865–6873. Retrieved from
556 http://www.ncbi.nlm.nih.gov/pubmed/1938891
557 Pum, Dietmar, & Sleytr, U. B. (2014). Reassembly of S-layer proteins. *Nanotechnology*.
558 https://doi.org/10.1088/0957-4484/25/31/312001
559 Quax, T.E.F., Daum, B. (2018) Structure and assembly mechanism of virus-associated
560 pyramids. Biophysical Reviews 2018 Apr;10(2):551-557. doi: 10.1007/s12551-017-
561 0357-4. Epub 2017 Dec 4. https://doi.org/10.1007/s12551-017-0357-4
562 Quemin, E.R.J., Lucas, S., Daum, B., Quax, T.E.F, Kühlbrandt, W., Forterre, P., Albers,
563 S.V., Prangishvili, D., Krupovic, M. (2013) First insights into the entry process of
564 hyperthermophilic archaeal viruses. Journal of Virology 87(24):13379-85.
565 https://doi.org/ 10.1128/JVI.02742-13

566 Rodrigues-Oliveira, T., Belmok, A., Vasconcellos, D., Schuster, B., & Kyaw, C. M. (2017).
567 Archaeal S-layers: Overview and current state of the art. *Frontiers in Microbiology*.
568 https://doi.org/10.3389/fmicb.2017.02597
569 She, Q., Zhang, C., Deng, L., Peng, N., Chen, Z., & Liang, Y. X. (2009). Genetic analyses
570 in the hyperthermophilic archaeon Sulfolobus islandicus . *Biochemical Society*
571 *Transactions*. https://doi.org/10.1042/bst0370092
572 Taylor, K. A., Deatherage, J. F., & Amos, L. A. (1982). Structure of the S-layer of
573 Sulfolobus acidocaldarius. *Nature*. https://doi.org/10.1038/299840a0
574 Tschitschko, B., Williams, T.J., Allen, M.A., Páez-Espino, D., Kyrpides, N., Zhong, L.,
575 Raftery, M.J., Cavicchioli, R. (2015). Antarctic archaea-virus interactions:
576 metaproteome-led analysis on invasion, evasion and adaption. ISME J., 9(9):2094-
577 2107. https://doi.org/10.1038/ismej.2015.110
578 Veith, A., Klingl, A., Zolghadr, B., Lauber, K., Mentele, R., Lottspeich, F., … Kletzin, A.
579 (2009). *Acidianus* , *Sulfolobus* and *Metallosphaera* surface layers: structure,
580 composition and gene expression. *Molecular Microbiology*, *73*(1), 58–72.
581 https://doi.org/10.1111/j.1365-2958.2009.06746.x
582 Zhang, C., Wipfler, R. L., Li, Y., Wang, Z., Hallett, E. N., & Whitaker, R. J. (2018).
583 Revealing S-layer Functions in the Hyperthermophilic Crenarchaeon Sulfolobus
584 islandicus. *BioRxiv*. https://doi.org/10.1101/444406
585
586
587
588
589
590
591
592
593
594
595
596
597
598

Figures

Figure 1

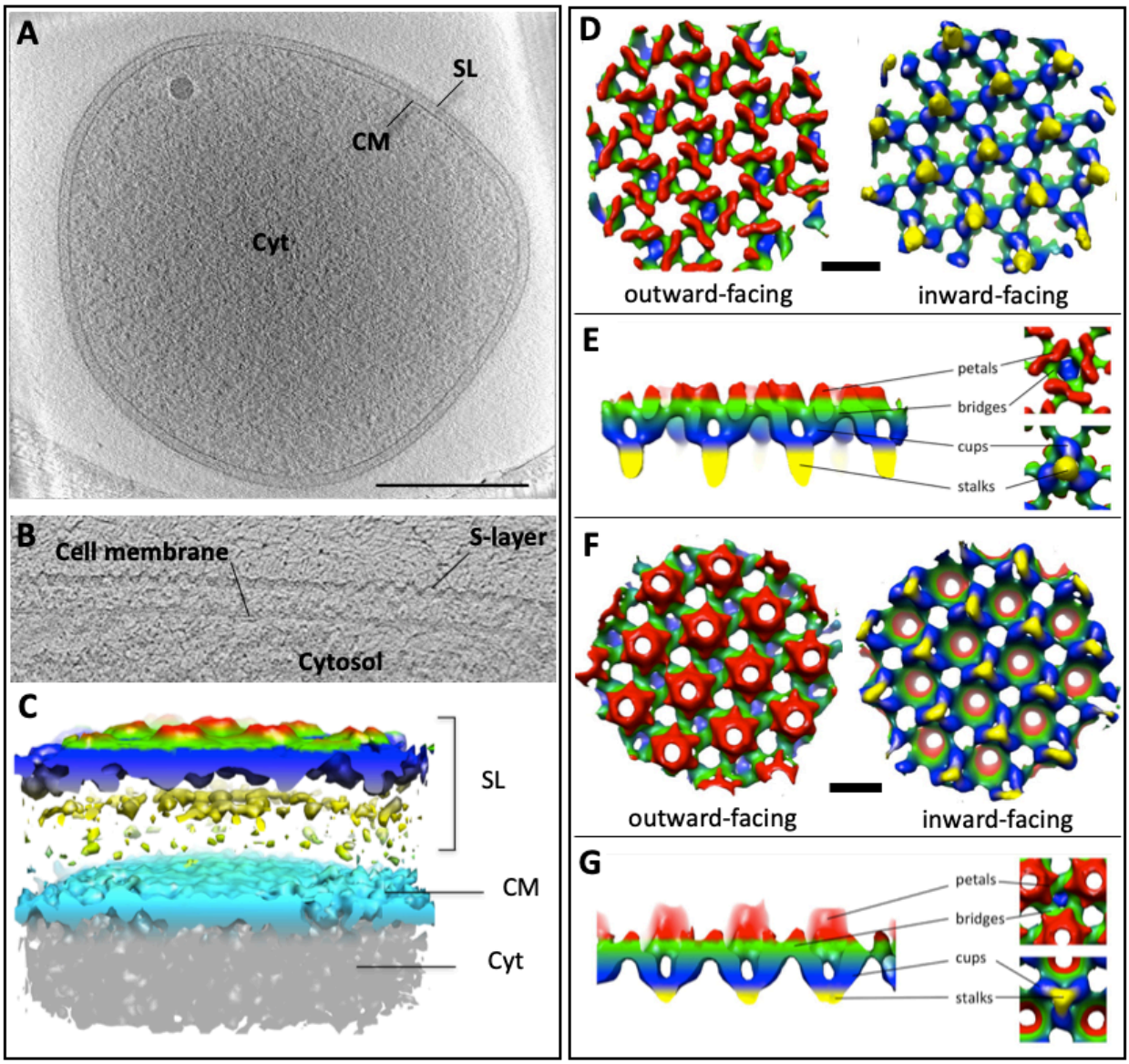

Figure 1 – Cryo electron tomography of *Sulfolobus* cells. A, tomographic slice through a *Sisl* cell. **B**, cross section through the cell membrane and S-layer. **C**, segmented surface representation of the *Sisl* S-layer. Scale bar (A), 500 nm. **D-G**, Sub-tomogram averages of *Saci* (D,E) and SisI (F,G) S-layers. Maps are coloured by proximity to the membrane plane. Yellow, proximal; red, distal. Scale bars (D, F), 20 nm.

Figure 2

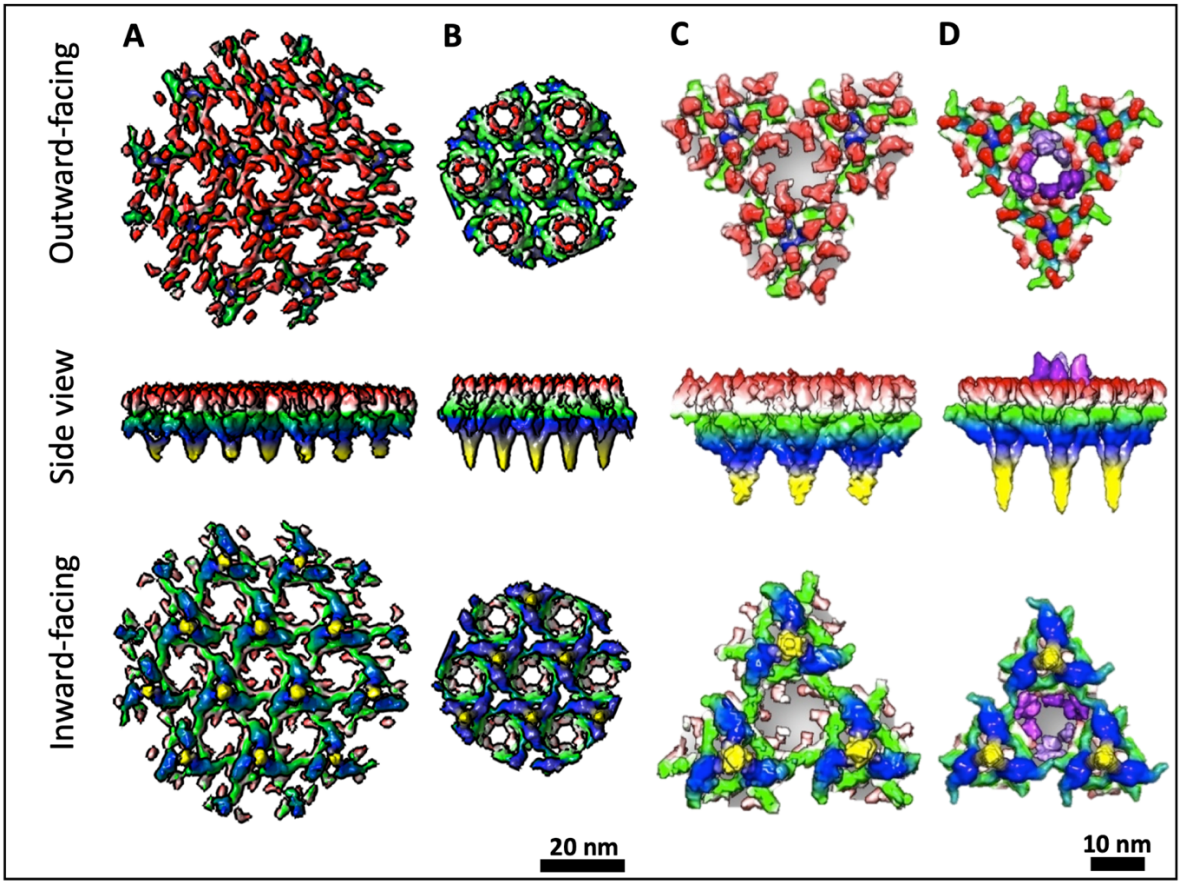

Figure 2 - Structure of isolated S-layers from *S. acidocaldarius* and *S. solfataricus*. A, **B**, S-layer maps of *Saci* (A) and *Ssol* (B) at 21 Å or 16 Å resolution, respectively. **C, D,** S-layer unit of *Saci* (C) and *Ssol* (D), including three stalks and a hexameric pore. Maps are coloured by proximity to the membrane plane. Yellow, proximal; red, distal; purple, conical protrusions. Scale bars, 20 nm.

Figure 3

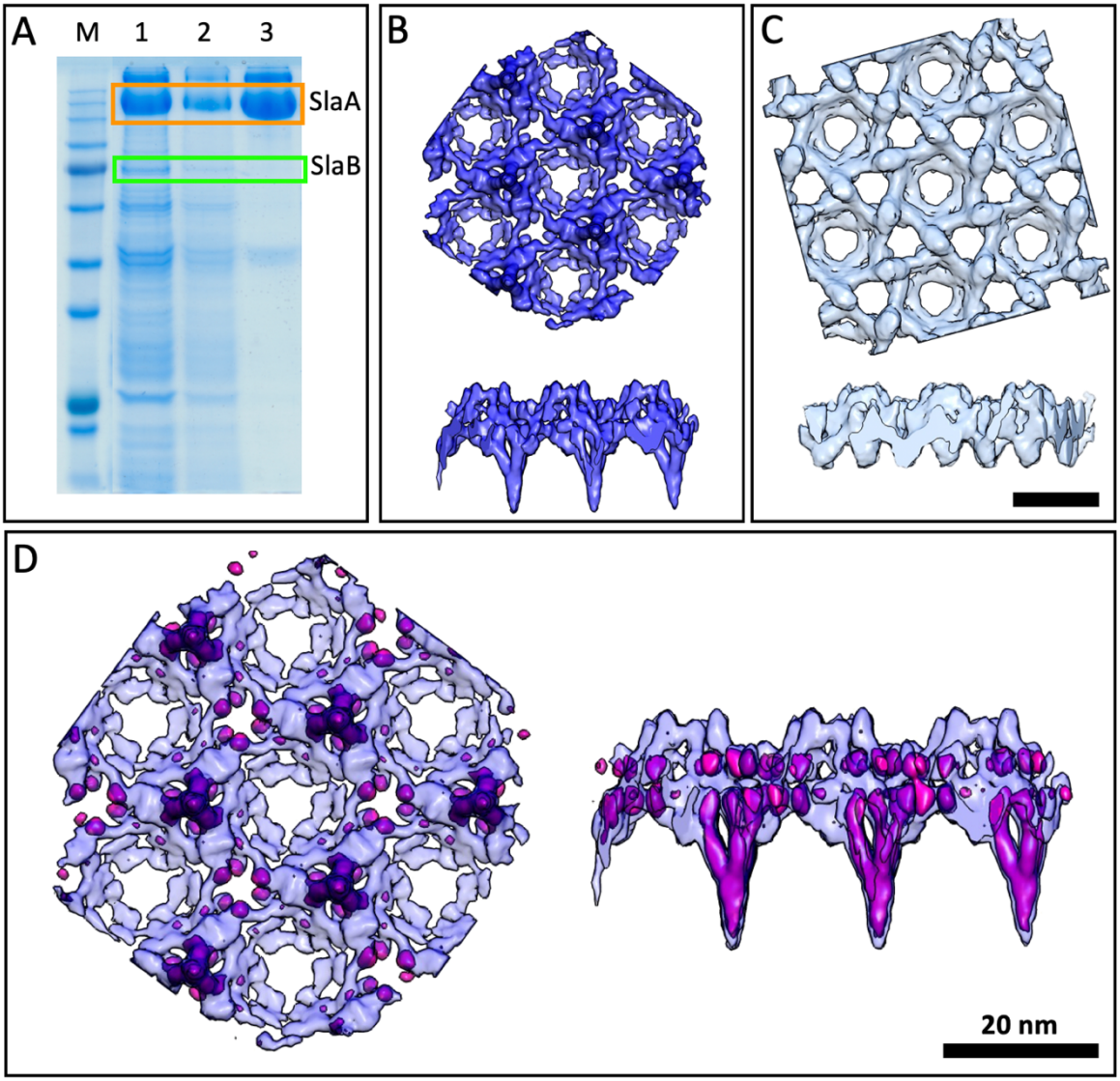

Figure 3 - Structural dissection of the *S. solfataricus* S-layer. A, SDS PAGE. M, marker; 1, washed once; 2, washed twice; 3, watched three times in detergent. **B**, sub-tomogram average of fully-assembled S-layer. **C**, sub-tomogram average of SlaB-depleted S-layer. **D**, difference map (pink) overlayed with the complete S-layer visualises location of SlaB.

Figure 4

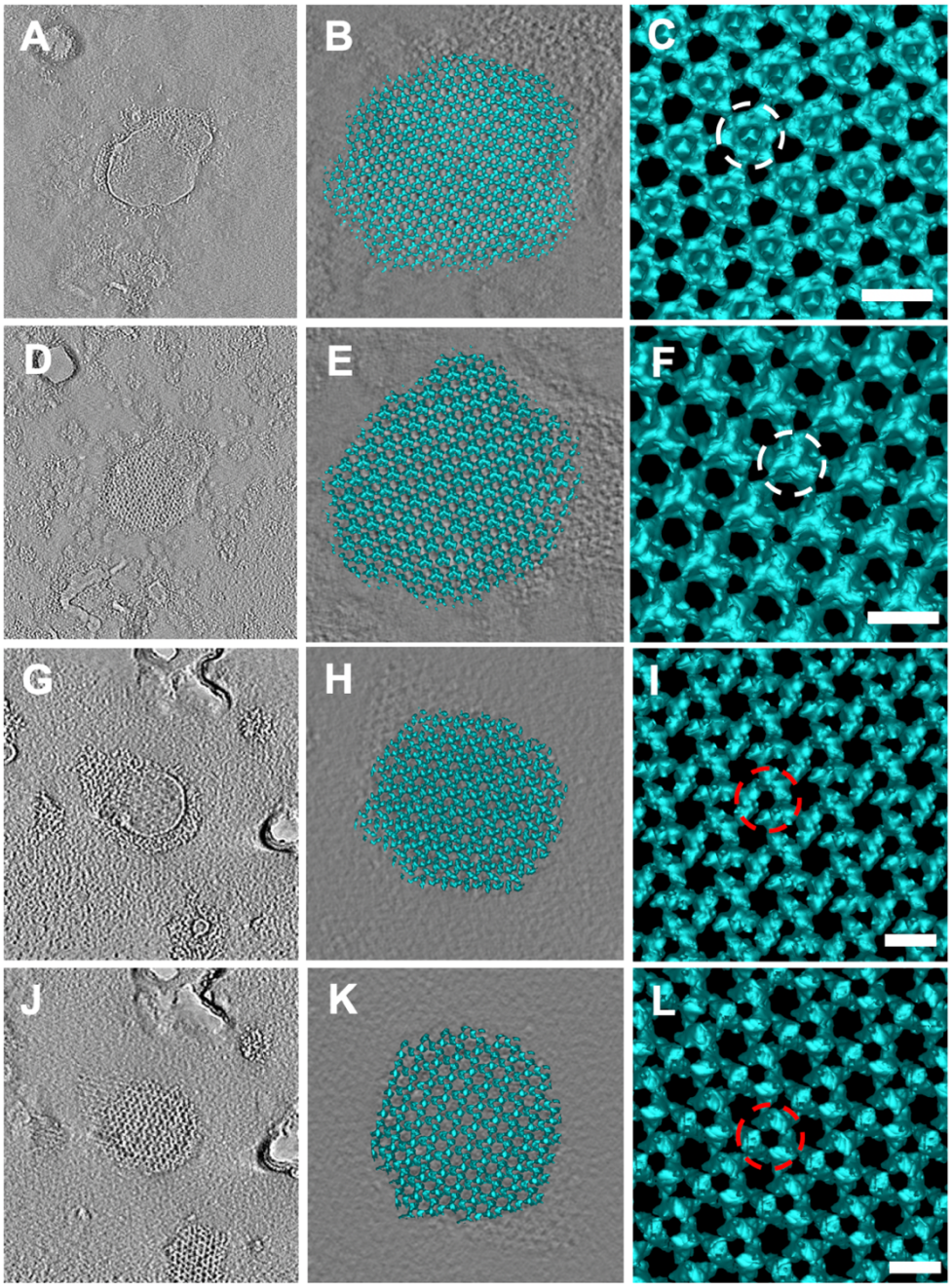

Figure 4 - S-layers recrystallise with and without SlaB. A-F, reassembly of *Sulfolobus* S-layers from SlaA and SlaB. G-L, reassembly of S-layers from SlaA only. (A,D,G,J, tomographic slices; B,E,H,K, 3D surface representation; C,F,I,L, sub-tomogram averages). White circle highlights presence of SlaB (C&F) and red circles absence of SlaB (I&L). Scale bar: 20 nm

Figure 5

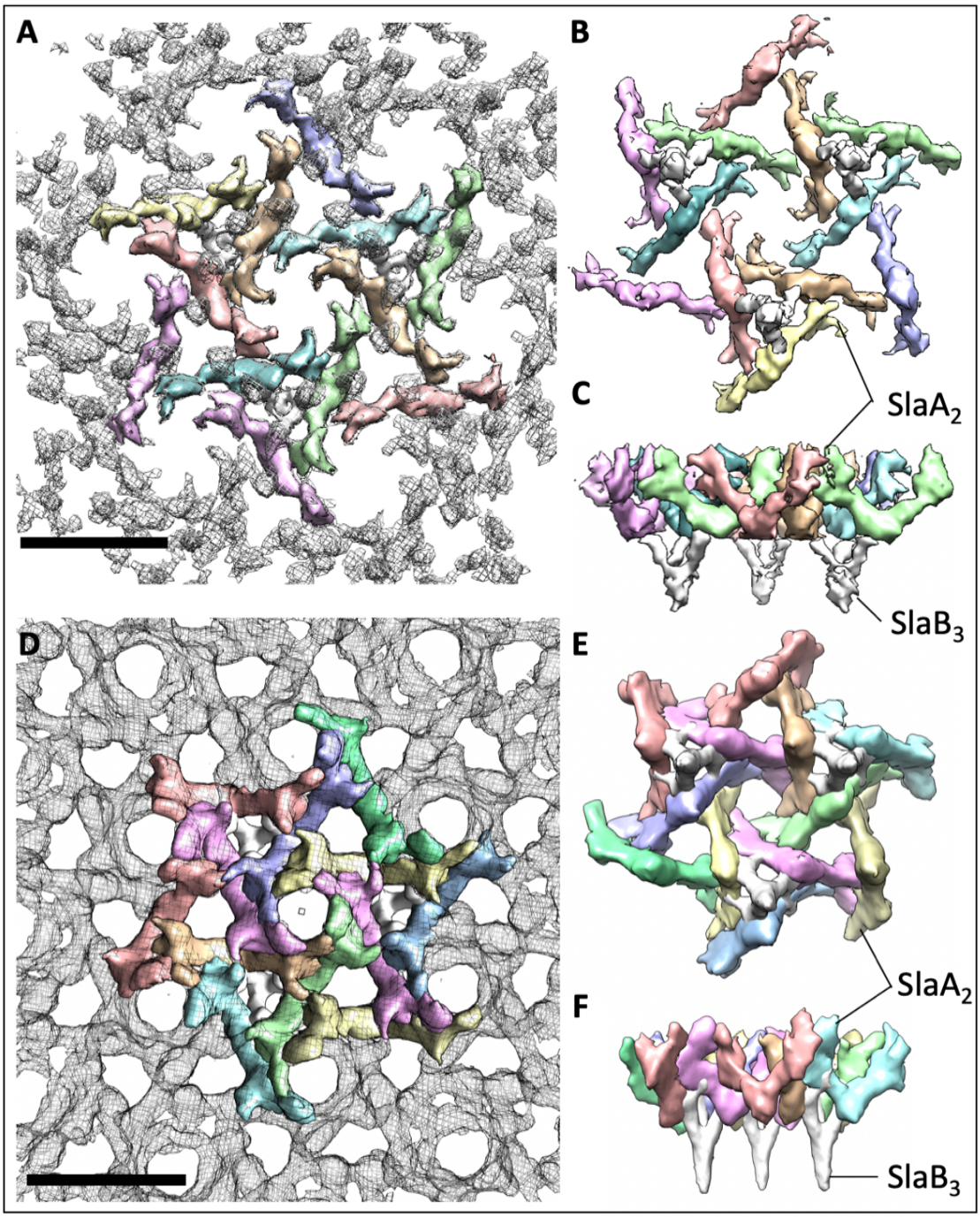

Figure 5 - Assembly models for the *S. acidocaldarius* (A-C) and *S. solfataricus* (D-F) S-layers. A, **D** outward facing surfaces (grey mesh) segmented into SlaA dimers (each dimer in a different colour) and SlaB trimers (white). **B**, **E** inward-facing surface. **C**, **F** side view, perpendicular to the membrane plane. Scale bar: 20 nm

Figure 6

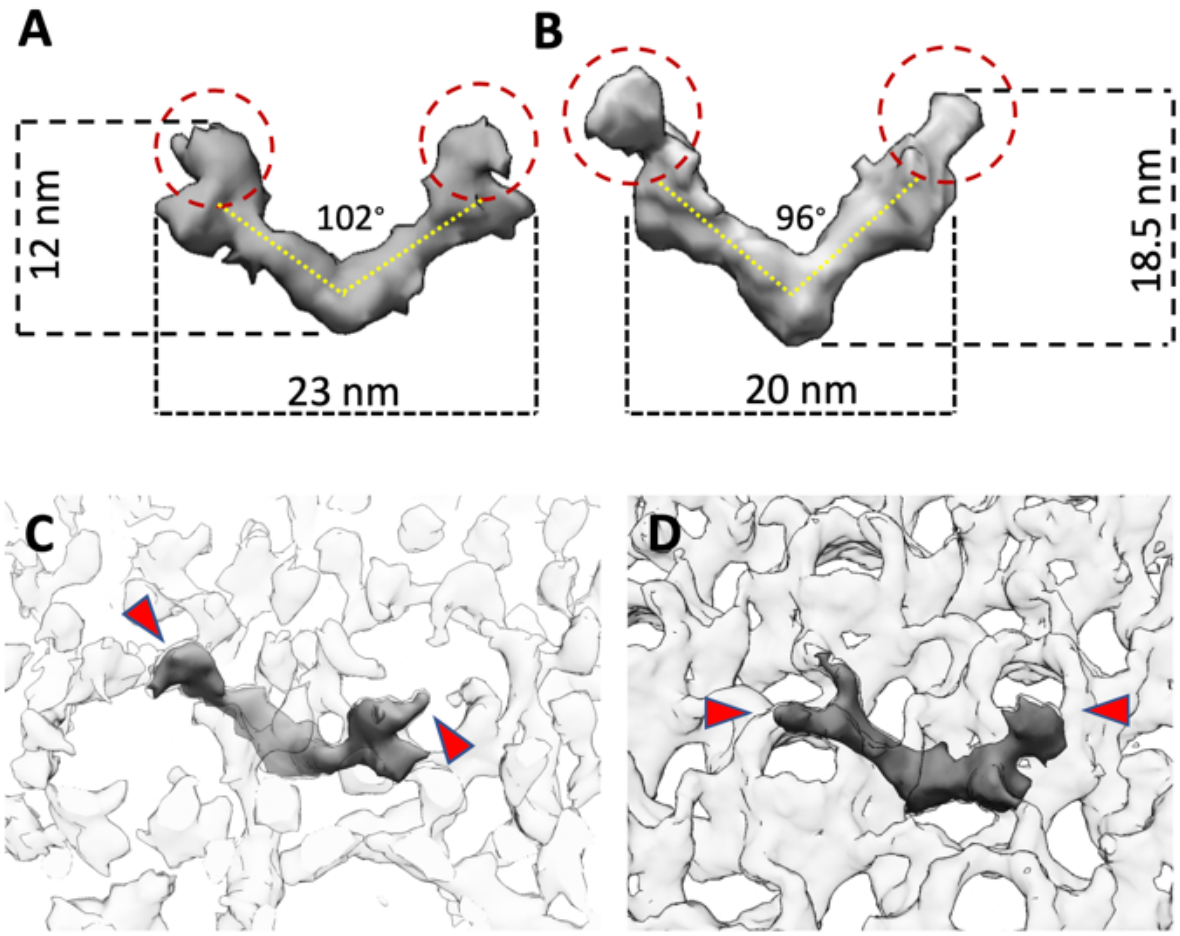

Figure 6 – SlaA structure determines S-layer topology and unit dimensions. Comparison of the structures of SlaA from *Saci* (**A**) and *Ssol* (**B**) show differences in length, height and angular shape of the dimer. **C, D**, location of one SlaA dimer within the S-layer of *Saci* (**C)** and *Ssol* (**D**). Red circles / arrowheads indicate apical domains that determine shape and topology of the hexameric pores.

Figure 7

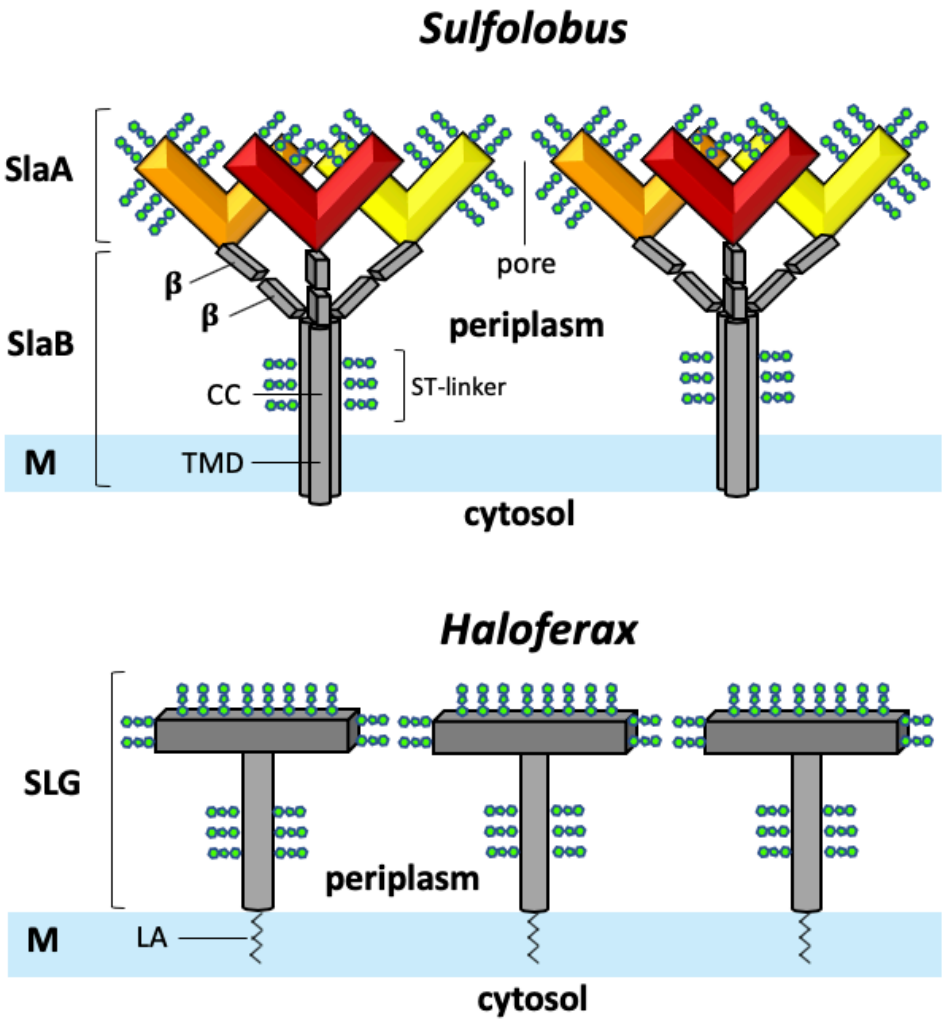

Figure 7 – Model of the *Sulfolobus* S-layer compared to the single-subunit S-layer of haloarchaea. The Sulfolobus S-layer (upper panel) consists of the two protein subunits: SlaA dimers (red, orange, yellow) form the outer S-layer canopy. Each SlaA protein is predicted to be rich in **β** strands. The SlaA dimer has a boomerang-like shape, the angle of which determines the S-layer unit cell size. SlaB trimers (grey) form the membrane anchors of the S-layer. Each SlaB is predicted to consist of an N-terminal transmembrane domain (TMD), a coiled-coil domain (CC) and 2-3 C-terminal **β**-sandwich domains (**β**). SlaA and SlaB proteins are highly glycosylated (green). In contrast, the S-layers of many halophile archaea (such as that of Haloferax volcanii; bottom panel) consist of multiple copies of only one S-layer glycoprotein (SLG) subunit and are inserted into the membrane by a posttranslationally added lipid anchor (LA).

Figure 1S1

A

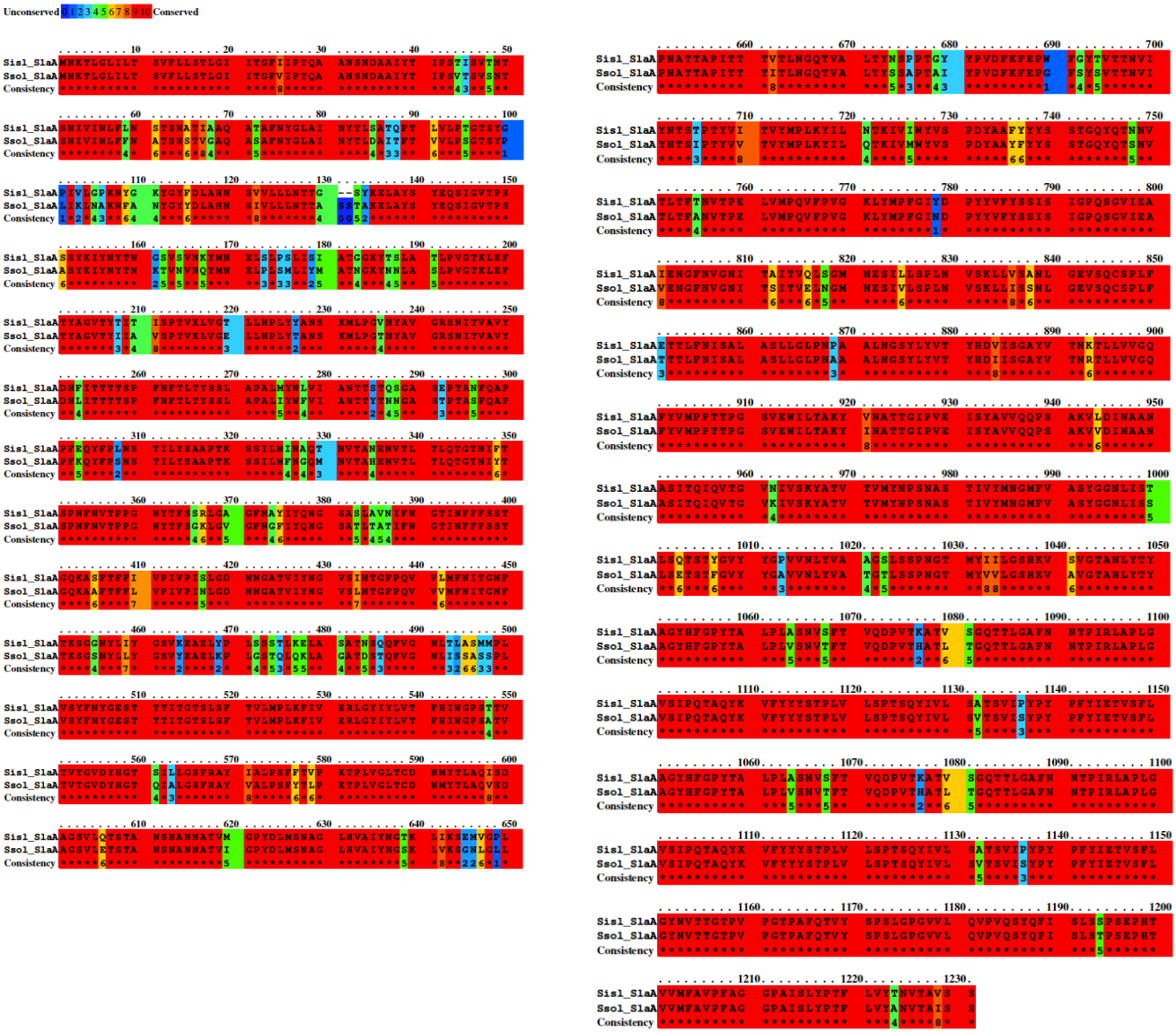
Unconserved 1 2 3 4 5 6 7 8 9 10 Conserved
Sisl_SlaA
Ssol_SlaA
Consistency

B

```
Unconserved 0 1 2 3 4 5 6 7 8 9 10 Conserved

           ..........10 ..........20 ..........30 ..........40 ..........50
Ssol_SlaB--MKKTFVLS TLILISVVAL VSTAVYTSGN VTFYSPSVNN QIYYVGKSVT
Saci_SlaBMVVKKTFVLS TLILISVVAL VSTAVYTSGN VTFYSPSVNN QIYYVGKSVT
Consistency 0 0 5******* ********** ********** ********** **********

           ..........60 ..........70 ..........80 ..........90 ..........100
Ssol_SlaBIDAVVPTQFA GQGAVINLFY PNSTLAASIP TTVNASGGIY VPNAYTFTNV
Saci_SlaBIDAVVPQQFA GQGAVINLFF PNSTLAASIP TTVNATGGIY VPNAYTFPHV
Consistency ******3*** *********6 ********** *****5**** *******34*

           ..........110..........120..........130..........140..........150
Ssol_SlaBIGIWQITVEV AGGVAVGTIN VNVTTPAIAP IILTLQNLAM YENNYPQFIE
Saci_SlaBIGIWQITVEV TGGVAVGTID VNVTTPAVAP IILTLQNLAM YENTYPQFIE
Consistency ********** 4********5 *******8** ********** ***4******

           ..........160..........170..........180..........190..........200
Ssol_SlaBLANGIITSVV MQNGTVNVMG YVYNTTVAPL SGAKVSLTLN IPSVGTETFT
Saci_SlaBFANGIITSVV MQNGTVNIMG YVYNSTVGPL SGATVSLTLN IPTVGTKTLS
Consistency 4********* ********8** ****5**4** ***3****** **5***5*45

           ..........210..........220..........230..........240..........250
Ssol_SlaBTTTAANGSFM LSFQVPQLST SLILISSYLI SGSLTISYGT HTVTYNVFIT
Saci_SlaBTTTASNGSFM LSFQVPQLST TLTLISSYLI SGSLTVSYGV HTVTYNVFIT
Consistency ****6***** ********** 5*3******* *****8***4 **********

           ..........260..........270..........280..........290..........300
Ssol_SlaBAIPNYLSVIN ALNTQVQTLK VEISSLNATI TSLNKSLANA NTQISTLQGE
Saci_SlaBAIPNYLSVIN ALNNEVSTLR SEISSLNSTI ASLNKSLANA NTQISNLQSE
Consistency ********** ***46*4**6 2******6** 4********* *****4**4*

           ..........310..........320..........330..........340..........350
Ssol_SlaBISNLNTEIGK LNSTVVSLSN QLASLSSQYT TLNNQVTALN AKIGNLSTSL
Saci_SlaBITTLNSEIGK LNSTVGSLST QLSSLSSQYN TLSSQVTALN GKISNLSTSL
Consistency *54**5**** *****1***4 **6******4 **55****** 4**4******

           ..........360..........370..........380..........390.....
Ssol_SlaBNNLSGEVASL KVTVSSLTTV AYGGIIAGII GLIVAIVAIV LVMRRIS
Saci_SlaBSTLNGEVASL RSTVSSLTTI AYGGIIAGII GLIVAIVAIV LVMRRIS
Consistency 54*5****** 62*******8 ********** ********** *******
```

Figure 1 S1 – Sequence alignment comparing SlaA (A) and SlaB (B) from *SisI* and *Ssol*. The sequence identity for SlaA and SlaB is 87.4% and 87.7%, respectively.

Figure 1S2

A

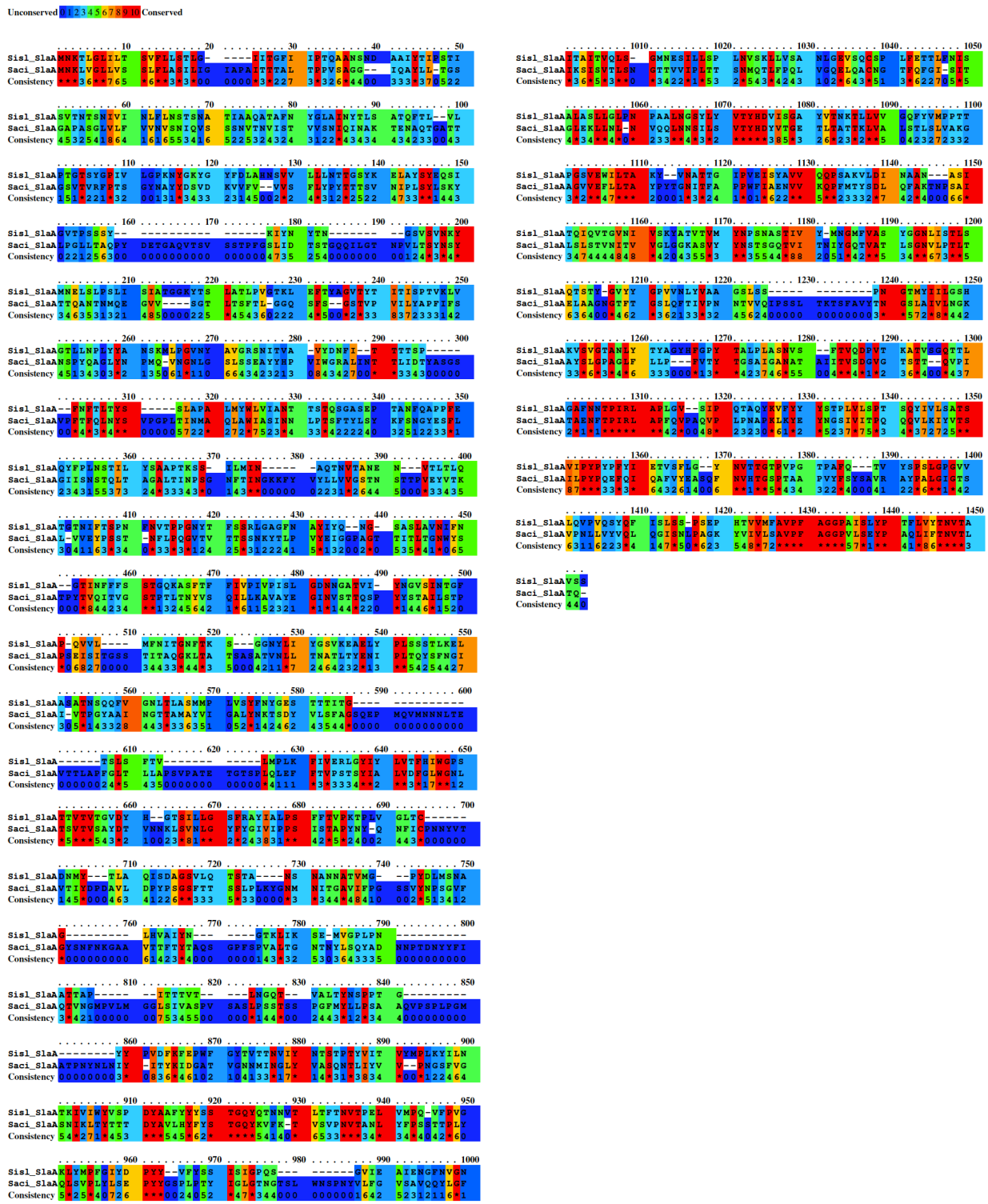
Unconserved 1 2 3 4 5 6 7 8 9 10 Conserved
Sisl_SlaA
Saci_SlaA
Consistency

B

```
Unconserved 0 1 2 3 4 5 6 7 8 9 10 Conserved

           ......... 10 ......... 20 ......... 30 ......... 40 ......... 50
Sisl_SlaBM-KKTFVLST LILISVVALV -STAVYT--- ---------- ------SGNV
Saci_SlaBMNKNLAILTP IVLLSLVLAP IAISAVTING ITFYSPVPNQ TYKYGQQLVL
Consistency *0*4328*53 78*7*6*332 063653*000 0000000000 000000401 6

           ......... 60 ......... 70 ......... 80 ......... 90 ......... 100
Sisl_SlaBTFYS-PSVNN QIYYVGKS-- -VTIDAVVPT QFAGQGAVIN LFYPNSTLAA
Saci_SlaBSIQSQPNALV TLYVYDPKGN VVYNNVYQTN SSGGLTATIA TFGSTPGFTT
Consistency 543*0*5511 37*33334 00 0*21553234 424*22*4*2 3*03432444

           ......... 110 ......... 120 ......... 130 ......... 140 ......... 150
Sisl_SlaBSIPTTVNASG G--------I YVPNAYTFTN VIGIWQ---- -----ITVEV
Saci_SlaBVGTYTVSLSV QGTTSESASV NVQYVPLTST ITATVVNQEG SPLAGATVQL
Consistency 2032**53*1 2000000008 1*31503254 8343020000 00000 3**66

           ......... 160 ......... 170 ......... 180 ......... 190 ......... 200
Sisl_SlaBA--------G GVAVGT---- -INVNVTTFA IAPIILTLQN LAMYENNYPQ
Saci_SlaBYNTTSGSNTL VATQTTNSQG VATFTVLSFP GVTQTFKLVA SLQGYAASTA
Consistency 2000000000 15422*0000 03434*3503 0531343*22 2340222233

           ......... 210 ......... 220 ......... 230 ......... 240 ......... 250
Sisl_SlaBFIELANGIIT S--------V VMQNGTVNVM GYVYNTT--- -VAPLSG---
Saci_SlaBSVSITGQQNA SVTITLVPAV VTIAPMYVIQ NGTVIGSGPS LSSIVVYQGL
Consistency 2847442114 *00000000* *3121331 84 4043125000 0261620000

           ......... 260 ......... 270 ......... 280 ......... 290 ......... 300
Sisl_SlaB--------AK VSLTLNIPSV GTETFTTTTA ANGSFMLSFQ VPQL--STSL
Saci_SlaBPAYILAQVSF AGQRVTTAPV SAQVYYPNGT QTVKASVITS GKYAGMYNIT
Consistency 00000000 61 542364333* 4464623424 3414236224 1333002423

           ......... 310 ......... 320 ......... 330 ......... 340 ......... 350
Sisl_SlaBILISSYLISG SLTISYGTHT VTYNVFITAI PNYLSVINAL NTQVQTLKVE
Saci_SlaBIMPPTESVQN YVFQLLIVAN YTTSSGQTLS TKYLMSVQAN QNLQALVNKE
Consistency *713522844 2621230424 3*25211*32 34**3284*1 4422336 42*

           ......... 360 ......... 370 ......... 380 ......... 390 ......... 400
Sisl_SlaBISSLNATITS INKSLANANT QISTLQGEIS NLNTEIGKIN STVVSLSNQL
Saci_SlaBISSLVQNITN LEKTVNNLQT QISTLNSSLS SLSQRITSLQ NTLASLNSTI
Consistency ****134**5 *4*562*34* *****4447* 5*534*24*4 5*65**5537

           ......... 410 ......... 420 ......... 430 ......... 440 ......... 450
Sisl_SlaBASLSSQYTTL NNQVTALNAK IGNLSTSLNN LSGEVASLKV TVSSLTTVAY
Saci_SlaBSSLSGTASSL SSQLNALQGK ISSLNSSITN LSGQLNSLQS KVNSLTPLVY
Consistency 6***43255* 55*64**44* *45*55*74* ***662**52 3*5***365*

           ......... 460 ......... 470 .....
Sisl_SlaBGGIIAGIIGL IVAIVAIVLV MRRIS
Saci_SlaBGGIIAGIIGL IVAIVAIVLV YRKIS
Consistency ********** ********** 3*6**
```

C

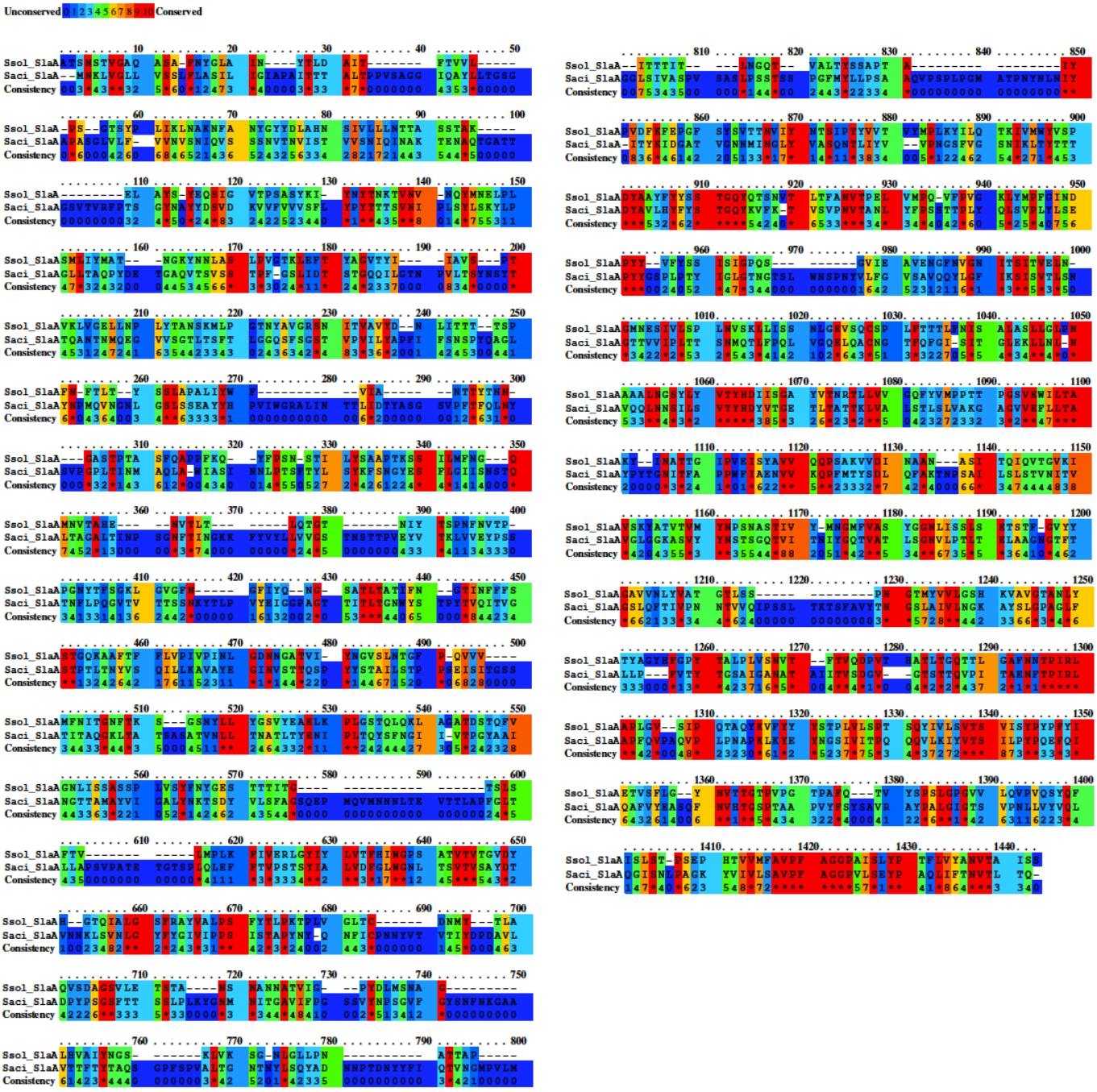
Unconserved 1 2 3 4 5 6 7 8 9 10 Conserved
Ssol_SlaA
Saci_SlaA
Consistency

D

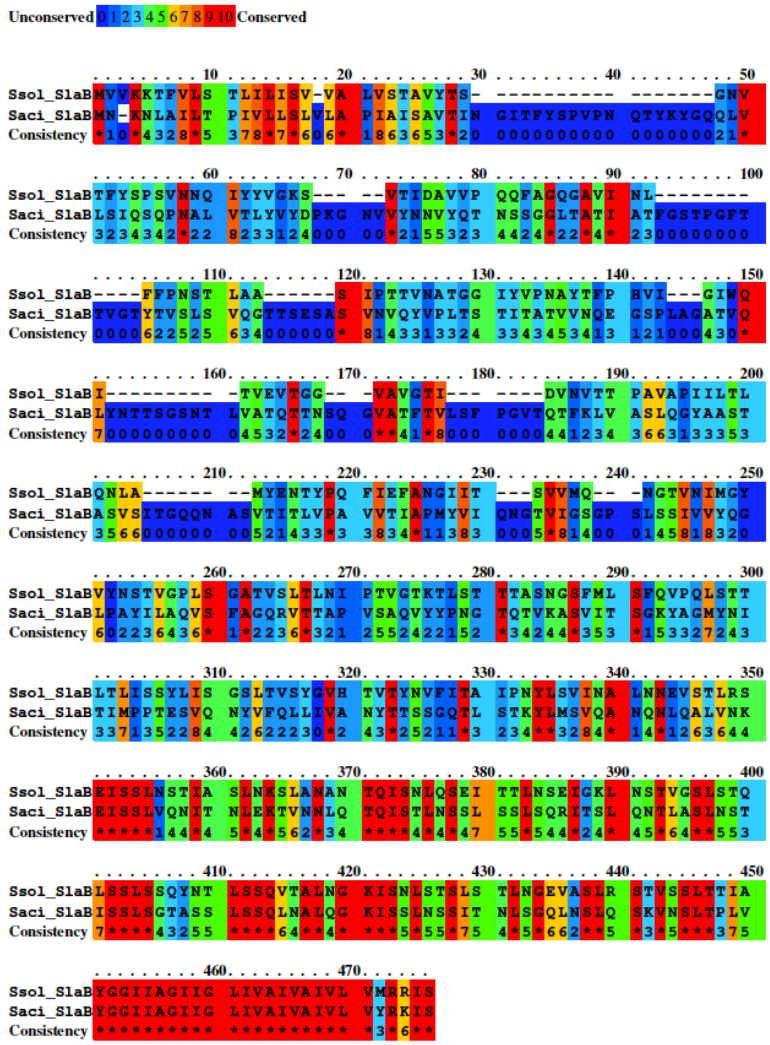

Figure 1 S2 – Sequence alignment comparing SlaA and SlaB from *Sisl*, *Ssol* and *Ssaci*. The sequence identity: *Sisl*_SlaA / S*aci*_SlaA, 24% (A); *Sisl*_SlaB / S*aci*_SlaB, 25% (B); *Ssol*_SlaA / S*aci*_SlaA, 25% (C); *Sisl*_SlaB / S*aci*_SlaB, 26% (D).

Figure 1S3

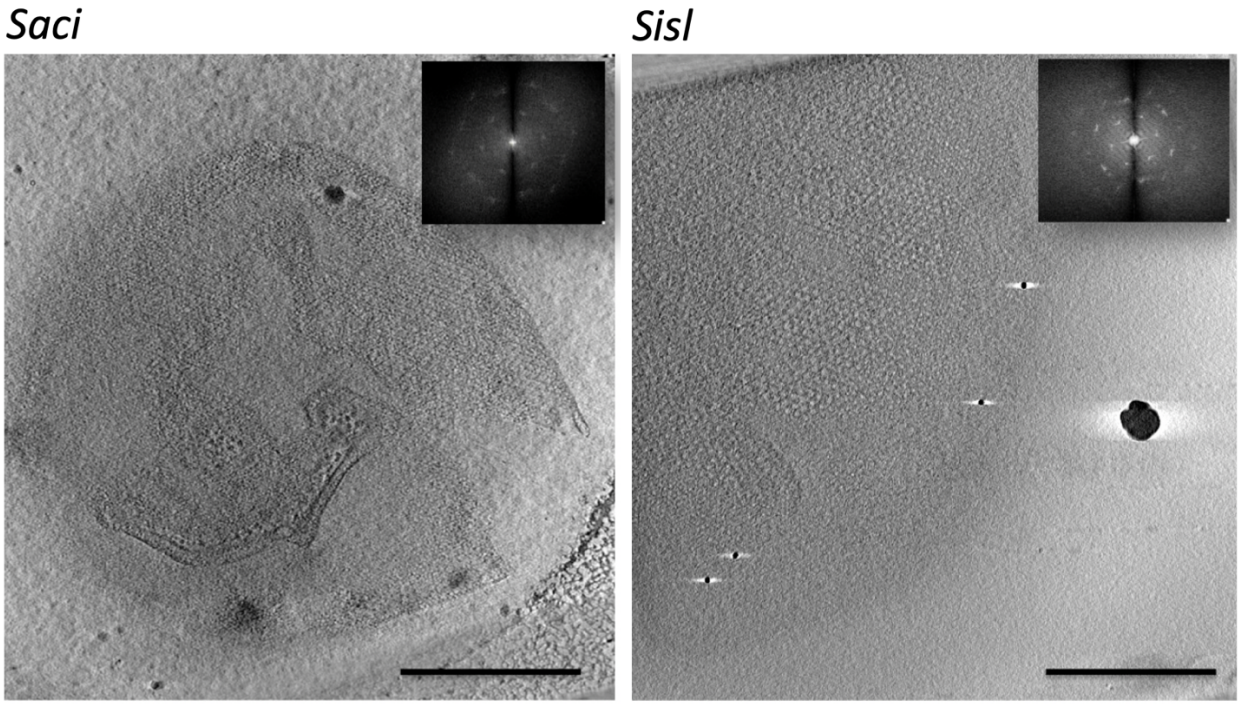

Figure 1 S3 – Tomographic slices through S-layer planes in whole-cell tomograms. Left panel, tomographic slice through the S-layer of Sulfolobus acidocaldarius; right panel, tomographic slice through the S-layer of Sulfolobus islandicus. Insets, power spectra reveal 2D lattices with hexagonal symmetry.

Figure 1S4

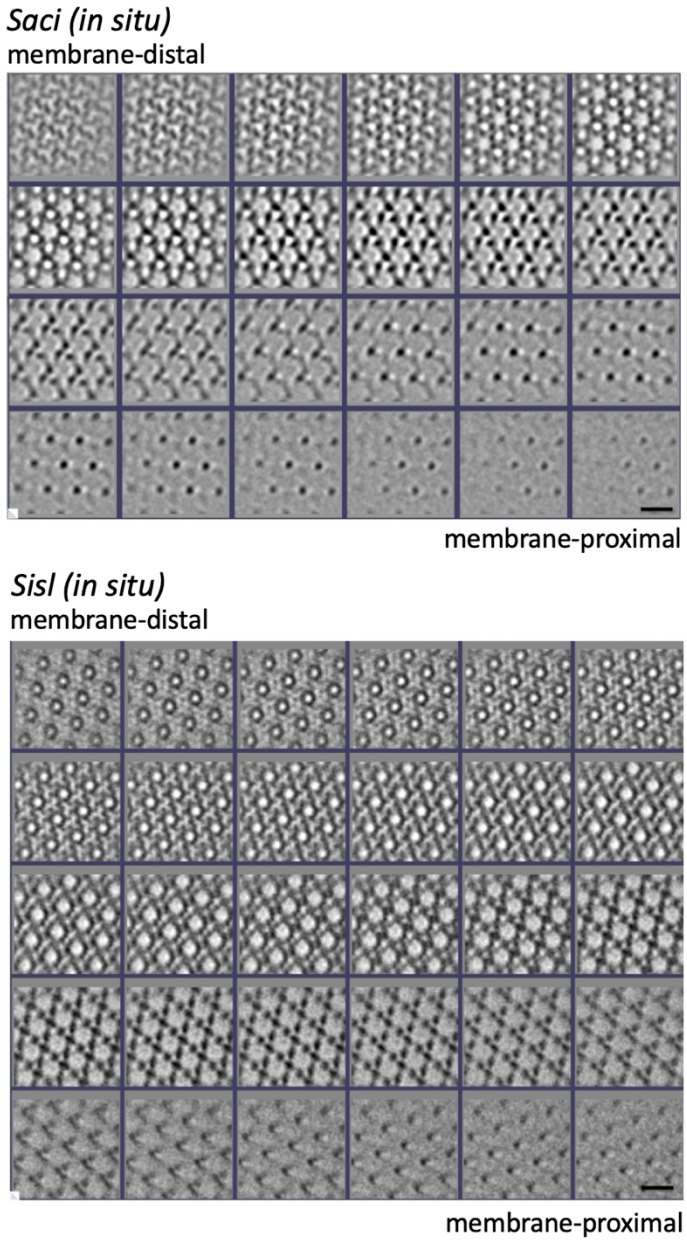

Figure 1 S4 – Consecutive slices through sub-tomogram averages of S-layers. Top panel, in situ map calculated from whole-cell tomogram of Sulfolobus acidocaldarius, bottom panel, map calculated from whole-cell tomogram of Sulfolobus islandicus.

Figure 1S5

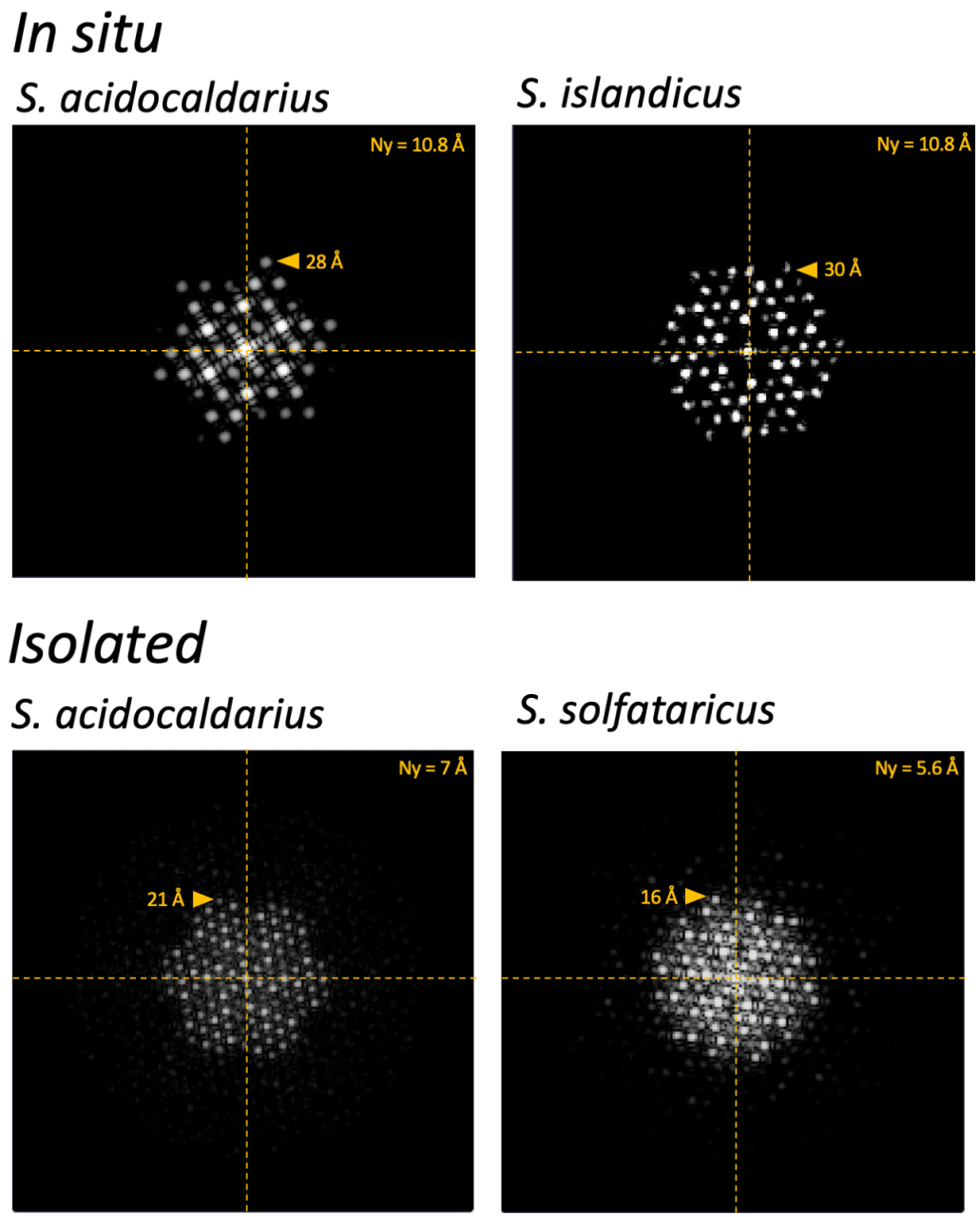

Figure 1 S5 – Resolution of S-layer maps determined by power spectra. Top panel, power spectra of in situ maps calculated from whole-cell tomograms, bottom panel, power spectra of maps calculated from isolated S-layers. Ny, Nyquist frequency